INTENSITY AND SHAPE DRIVEN LEVEL SET FOR MEDICAL IMAGE SEGMENTATION

A thesis submitted in fulfilment of the requirements for the degree of

Master of Engineering in Electronics and Telecommunication Engineering

by

Pranavesh Banerjee
Examination Roll No. : M4ETC19005
Registration No. : 140688 of 2017-2018

Under the supervision of

Prof. Ananda Shankar Chowdhury
Department of Electronics and Tele-Communication Engineering
Jadavpur University

May 2019

Faculty of Engineering and Technology
Jadavpur University

Certificate of Recommendation

This is to certify that the thesis entitled "Intensity and Shape driven Level Set for Medical Image Segmentation" has been carried out by "Pranavesh Banerjee" (Examination Roll no. : M4ETC19005 and Registration no. : 140688 of 2017-2018) under my guidance and supervision and be accepted in partial fulfilment of the requirements for the degree of *Master of Engineering in Electronics and Telecommunication Engineering*.

Supervisor

Dr. Ananda Shankar Chowdhury
Professor
Department of Electronics and Telecommunication Engineering
Jadavpur University

Head of the Department

Dr. Sheli Sinha Chaudhuri
Professor
Department of Electronics and Telecommunication Engineering
Jadavpur University

Prof. Chiranjib Bhattacharjee
Dean
Faculty of Engineering and Technology
Jadavpur University

Faculty of Engineering and Technology
Jadavpur University

Certificate of Approval

The thesis entitled

Intensity and Shape driven Level Set for Medical Image Segmentation

by

Pranavesh Banerjee

Examination Roll No. : M4ETC19005

Registration No. : 140688 of 2017-2018

is approved for the degree of

Master of Engineering in Electronics and Telecommunication Engineering

Signature of Examiner

Signature of Supervisor

Date : _____

Place : _____

Declaration

I hereby declare that my thesis contains literature survey and research work in my own words and is truly in accordance with academic ethics and educational integrity. With my sole responsibility I would like to mention that none of the ideas, facts and results represented in the thesis have been fabricated or falsified. I have cited the original resources as required. I understand that non-compliance of any of the above can evoke strict disciplinary action.

Signature of student

_____

Name : Pranavesh Banerjee

Examination Roll No. : M4ETC19005

Registration No. : 140688 of 2017-2018

Acknowledgement

I would extend my sincere gratitude and heartfelt indebtedness to my research supervisor, Dr. Ananda Shankar Chowdhury, Professor of Department of Electronics and Telecommunication Engineering, Jadavpur University, for his kind supervision. The unique guidance and support I received have helped me to work freely and thereby explore the world of research to my utmost satisfaction. Without him this project would not have been possible.

I am thankful to Prof. Dr. Sheli Sinha Chaudhuri, Head of the Department of Electronics and Telecommunication Engineering, Jadavpur University, for providing me all the necessary facilities to carry out this project.

I am also grateful to all the members of our group "Imaging, Vision and Pattern Recognition (IVPR)", especially Rukhmini Roy, Arindam Sikdar and Abhimanyu Sahu for their constant help and encouragement.

I also thank my friends for helping me in various ways.

Finally, I would thank my parents, Mr. Barun Banerjee and Mrs. Sibani Banerjee, for their sacrifice and tolerance that have paved the royal road of my education, their love and support inspired me to stay focussed in my work all the time. I also thank my other beloved family members for their constant encouragement throughout the entire course.

Abstract

Level set methods are widely used in the computer vision and image processing communities. Existing level set methods for biomedical image segmentation are mostly limited to specific applications. Moreover, medical image segmentation becomes challenging due to several factors like low contrast images, presence of noise, variability in the shape of lesions, presence of similar intensity structures as lesions. Considering these challenges, we propose a more generic level set segmentation method in this thesis which can segment different types of lesions/regions from medical images. The zero level set of the proposed level set framework is improved by using three different functions namely a constant function, a step function and a Gaussian function. These three different initialization are used as per the nature of the lesions present in medical images. For example, constant and step initialization are used when there are multiple lesions present in the image but a constant function results in false segmentation as it gives similar priority to all the regions having similar intensity whether it is a lesion or not. A step initialization has two different values one within the region and other outside the region to be segmented but it gives equal priority to similar intensity structures which results in false segmentation as well. To prevent this, a Gaussian level set initialization is introduced which gives higher priority only to the lesion/region to be segmented which in turn reduces the false segmentation. The initialization is robust in nature *i.e.*, the contour evolution of the proposed zero level set does not depend on the position of initialization. The second contribution of the proposed framework is that it mines the intensity and shape information of the image to be segmented in an automated fashion and sets the parameters of the level set evolution. The intensity term is incorporated to handle the segmentation of low-contrast images and it also helps in the segmentation of multiple regions having similar intensity. The shape information is introduced as a weight factor in the proposed level set framework based on the circularity of the evolving contour to prioritize the circular and non-circular lesion to be segmented. This in turn helps in the accurate segmentation of different types of lesions present in the image. In this work, we have chosen three different applications namely lung nodule segmentation, Brain tumour segmentation and cell segmentation. Experiments on the publicly available LIDC/IDRI dataset, BRATS 2015 dataset and BBBC dataset clearly reveal that our method achieves promising results compared to several state-of-the-art competitors.

Contents

List of Figures

List of Tables

Abbreviation

CAD : **C**omputer **A**ided **D**iagnosis

CNN : **C**onvolutional **N**eural **N**etwork

CT : **C**omputed **T**omography

GT : **G**round **T**ruth

LSF : **L**evel **S**et **F**unction

MRI : **M**agnetic **R**esonance **I**maging

PDE : **P**artial **D**ifferential **E**quation

SDF : **S**igned **D**istance **F**unction

Chapter 1

INTRODUCTION

This chapter describes the basics of level set and its different applications followed by the organization of the thesis.

1.1 Basics of Level Set

A segmentation problem can be modeled as finding suitable curve(s) which would enclose regions of interest. Intuitively, we can obtain these curves directly using control points. However, there are issues involved in updating the control points. For example, if two separate closed curves needed to merge into one, or one needs to split into two, then when and how would this merge or split take place? If control points are too close together, should they be merged? If not, then how would an algorithm detect when to merge or split? After this is detected, data structures for the curve(s) needs to be updated as well.

The concept of level set was first presented by Osher and Sethian [1] for front propagation to model ocean waves and burning flames [2]. Malladi applied it for medical imaging purposes [3]. The idea of level set is to embed a curve within a surface. This is done by recognizing a curve or contour as a particular level of a surface. In simple terms, if we have a plane that cuts through a three dimensional surface, we would get curves, which are the lines of intersection between them. When curves are represented in that way, the above mentioned problems of splitting and merging curves are addressed without the need to treat them as special cases. Figure 1.1 shows a circle embedded within a conical surface. Figure 1.2 shows how a curve splits into two by moving along the surface of the level set.

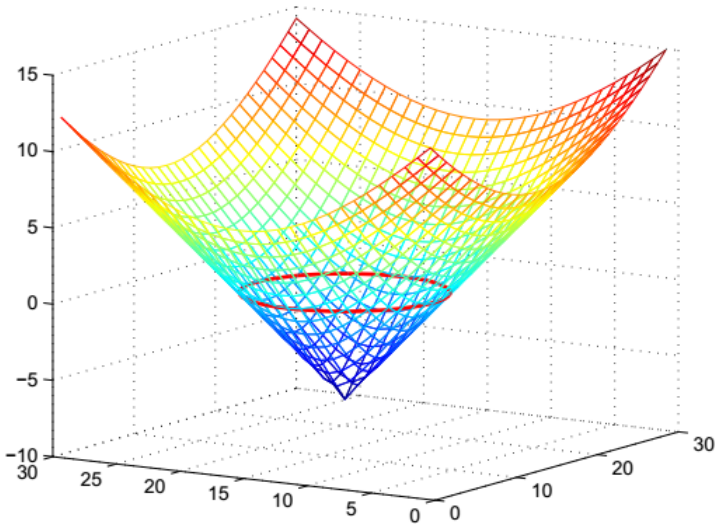

Figure 1.1: Circle embedded within a cone

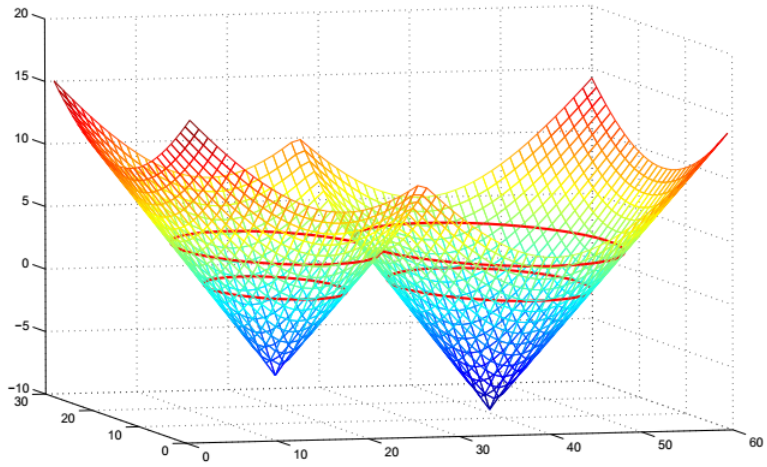

Figure 1.2: Splitting and Merging of contours when part of a surface

Formally, level-set methods are a conceptual framework to use level sets as a tool for numerical analysis of surfaces and shapes. The advantage of the level set model is that one can perform numerical computations involving curves and surfaces on a fixed Cartesian grid without having to parameterize these objects [4]. Also, the level-set method makes it very easy to follow shapes that change topology [5], for example, when a shape splits in two, develops holes, or the reverse of these operations. This makes the level-set method a great tool for modelling time-varying objects, like inflation of an airbag.

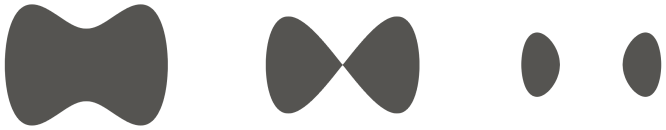

(a) Changing topology in 2-D

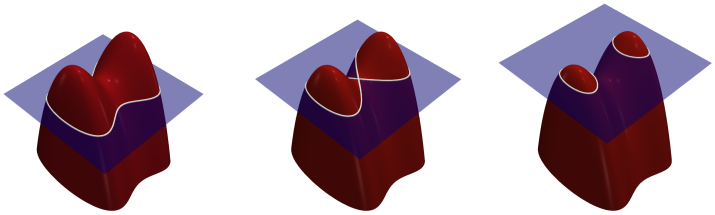

(b) Changing topology in 3-D

Figure 1.3: Changing topology in 2-D captured as part of a surface in 3-D

In the figure 1.3a , we see a curve changing its topology by splitting in two. It is quite hard to describe this transformation numerically by parameterising the boundary of the curve and following its evolution. We need an algorithm to detect the moment when curve splits in two, and then construct parameters for the two newly obtained curves. On the other hand, if we look at the figure 1.3b, we see that the level set function merely translated downwards. This is an example which shows that it is much easier to work with a evolving or moving curve through its level-set function than with such curves directly. Working on the curve directly means, we need to consider and handle all possible deformations the curve might undergo.

1.2 Applications of Level Set

Level set methods are mostly used in the following applications

- Computational fluid dynamics
- Trajectory planning
- Biophysics
- Image processing

Computational Fluid Dynamics (CFD) is a theoretical method of scientific and engineering investigation, which is concerned with the development and application of a virtual video-camera like tool —a software which is used to analyse a fluid dynamics, heat and mass transfer problem for a unified cause-and-effect study [6]. Here, the software results in a fluid-dynamic movie where each picture demonstrates a flow property like pressure, velocity, temperature and stream-function. The main objective is a scientific understanding and engineering related study and analysis for fluid dynamics problems. Representation as well as mathematical-modelling of flow is needed to create such a fluid-dynamic movie. Level set methods are an excellent way to represent and mathematically model such fluid dynamics simulation. The resulting movie for flow-properties and interface give a detailed spatial and temporal fluid-dynamic information, which greatly helps in a scientific and engineering investigation.

Planning a path in a complex environment is a very old problem. Earlier prior knowledge, however limited, was the only way employed to make predictions for such planning [7]. Today, in contemporary science and engineering, modelling and computational approaches that optimize an objective function, are utilized to plan paths. Level set is one of the methods that are being used for path planning.

Biophysics and biomechanics are two fields where Fluid-Structure interactions play an important role, both from computing and modelling point of view. In many 3-D applications, flow and solid models coexist in a biochemical system [8]. For such problems, it is desirable to have computing tools, which could readily couple models of different nature, and hence a call for level sets.

Image processing is a method to convert an image into digital form and perform some operations on it, in order to get a modified or enhanced image or to extract some useful information from it. Image Processing system includes treating images as two or three dimensional signals and applying signal processing methods to them [9]. Image processing is an umbrella term that has many constituents. Image segmentation, an important constituent of image processing, plays an important role in many medical fields e.g. identifying anatomical structures, diagnosis and surgery etc. Generally an image segmentation is a process of partitioning an image into overlapping or non-overlapping constituent regions which are distinct based on some characteristics e.g. intensity, color, texture, etc. The goal of segmentation is to simplify and/or change the representation of an image into something that is more meaningful and easier to understand and analyze. Level set is one well known method used in image segmenting.

1.3 Organization of the Thesis

The thesis is organized into six chapters. Here is a glimpse:
Chapter 1 introduces the basics of –Level Sets.
Chapter 2 covers the theoretical foundations of level sets and discusses the implementation issues.

Chapter 3 provides an extensive literature review, points out the shortcomings of these works and highlights the contributions.
Chapter 4 describes the proposed framework with necessary details.
Chapter 5 presents the experimental results with a thorough analysis.
Chapter 6 concludes the work with outlines for future research.

Reference

[1] S. Osher and R. Fedkiw, 2006. Level set methods and dynamic implicit surfaces (Vol. 153). Springer Science & Business Media.

[2] J. A. Sethian, 1999. Level set methods and fast marching methods: evolving interfaces in computational geometry, fluid mechanics, computer vision, and materials science (Vol. 3). Cambridge university press.

[3] R. Malladi, J. A. Sethian and B. C. Vemuri, 1994. Shape modeling with front propagation: A level set approach.

[4] S. Osher and J. A. Sethian, 1988. Fronts propagating with curvature-dependent speed: algorithms based on Hamilton-Jacobi formulations. Journal of computational physics, 79(1), pp.12-49.

[5] J. A. Sethian, 1996. Theory, algorithms, and applications of level set methods for propagating interfaces. Acta numerica, 5, pp.309-395.

[6] A. Sharma, 2015. Level set method for computational multi-fluid dynamics: A review on developments, applications and analysis. Sadhana, 40(3), pp.627-652.

[7] T. Lolla, M. P. Ueckermann, K. Yigit, P. J. Haley and P. F. Lermusiaux, 2012, May. Path planning in time dependent flow fields using level set methods. In 2012 IEEE International Conference on Robotics and Automation (pp. 166-173). IEEE.

[8] E. Maitre, T. Milcent, G. H. Cottet, A. Raoult and Y. Usson, 2009. Applications of level set methods in computational biophysics. Mathematical and Computer Modelling, 49(11-12), pp.2161-2169.

[9] R. Tsai and S. Osher, 2003. Level set methods and their applications in image science. Communications in Mathematical Sciences, 1(4), pp.1-20.

Chapter 2

THEORETICAL FOUNDATIONS

In computer vision, recognising objects often depends on identifying a particular shape or shapes in an image. This is a difficult task and a central problem in vision [1]. Image segmentation is concerned with finding ways of extracting objects from a given image that are sufficiently general to be useful for a range of shapes, while at the same time maintaining sufficient accuracy for a given class of image data [2]. To start with, it is necessary for us to know the basic concepts for better understanding the ideas and the proposed work. This chapter introduces the basic and common terminologies and the related theory used in the formulation and also a part of the literature.

2.1 Active Contour : A moving curve

The basic idea of any active contour is to start with initial boundary or shape represented in a form of an open or closed curve or contours, and iteratively modify them by applying shrink or expansion operations according to the conditions given and constraints of the image. These shrink and expansion operations, called contour evolution, are generally performed by the minimization of an energy functional [3]. Active contours have been widely used for applications like object tracking, shape recognition, image segmentation, edge detection and stereo matching.

There are two main approaches in active contours based on the mathematical implementation

- Snakes
- Level Sets

Snake model have a very simple form. They consist of a set of control points, connected by straight lines. Each control point has a position, given by an (X, Y) coordinate in the image. In other words, a snake is entirely specified by the number and coordinates of its control points. Adjustments of the snakes are made by moving these control points. In general, snakes can be open or closed loops in an image. Snakes explicitly move the predefined points based on an energy minimization scheme [4].

Level set theory, a formulation to implement active contours, was proposed by Osher and Sethian [5]. The use of level set theory has provided more flexibility and convenience in the implementation of active contours.

2.2 Level Set : Implementation of Active Contour

Level set approaches move contours *implicitly* as a particular level of a function. This means that the change in the contour shape and size is a reflection of the change in the underlying level set function. This way of representing the motion of a contour is possible only when we are able to represent a curve or contour *implicitly* as a particular level of a higher dimensional function.

2.2.1 Implicit and Explicit function in Level Set theory

The concept is best explained by an example. Suppose we divide the real line in one spatial dimension into three distinct parts by the points x = –1 and x = 1. Now let us define $(-\infty,-1),(-1,+1)$ and $(1,\infty)$ as three separate sub-domains of interest and regard the first and third as two disjoint parts of the same region. We refer to $\Omega^- = (-1,+1)$ as the inside part of the domain and $\Omega^+ = (-\infty,-1)\cup(1,\infty)$ as the outside part of the domain. The border which discriminates or divides the inside and the outside regions essentially consists of the two points, *i.e.* $\partial\Omega = \{-1,+1\}$ and is called the interface. In one spatial dimension, the inside and outside regions are *one-dimensional* objects, whereas the interface is less than one-dimension, that is, the points making up the interface are *zero-dimensional*. In general, for any R^n dimensional region, sub-domains are n-dimensional, while the interface has dimension of n-1. In other words, the interface are of co-dimension one. This way of representing an interface is called *explicit representation*, where we explicitly note down the co-ordinates or points [6].

Alternatively, an *implicit interface representation* defines the interface as an iso-contour of a function. In the above stated example, the zero iso-contour of $\phi(x) = x^2 - 1$ is the set of all points where $\phi(x) = 0$, *i.e.*., which is exactly $\partial\Omega = \{-1,+1\}$. This is shown in figure 2.1a. Note that the implicit function $\phi(x)$ is defined throughout the one-dimensional domain, whereas the iso-contour defining the interface is one dimension lower. In general, for any R^n domain, the implicit function $\phi(x)$ defined on all R^n, has iso-contour of dimension n-1. Similarly, in three spatial dimensions, our lower-dimensional interface is a curve. As for example, consider the surface defined as $\phi(x,y) = x^2 + y^2 - 1$, where the interface defined by the $\phi(x,y) = 0$ isocontour is a unit circle as shown in figure 2.1b.

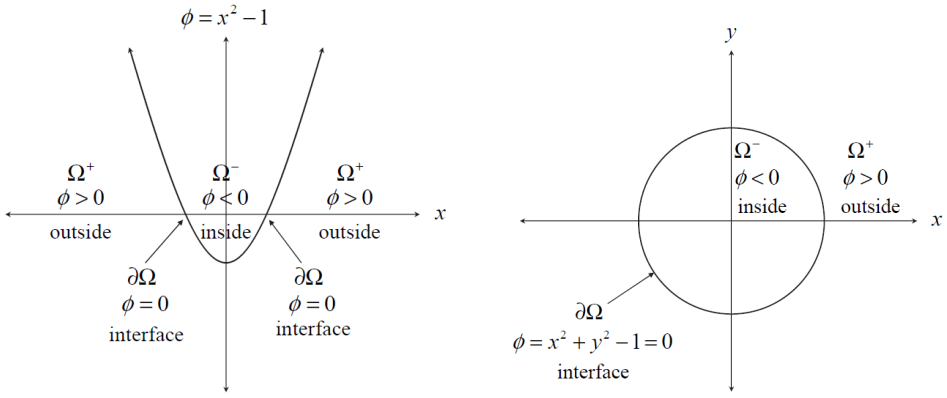

(a) Implicit function defining points (b) Implicit function defining circle

Figure 2.1: Implicit Functions

In *Level Set* formulation, a moving contour in two-dimensional space is intrinsically represented as a particular *level* of an evolving three dimensional function.

2.2.2 Comparison of Implicit and Explicit representation

Implicit functions make both simple Boolean operations and more advanced constructive solid geometry (CSG) operations easy to apply. This is important for CAD. One distinct feature of $\phi(\vec{x}) = 0$ isocontour of being an interface is that, we can determine on which side of the interface a point is simply by looking at the local sign of ϕ. In other words, $\vec{x}$ is inside the interface when $\phi(\vec{x}) > 0$ and outside the interface when $\phi(\vec{x}) < 0$ or vice-versa depending on how ϕ is defined. With an explicit representation of the interface it is difficult to determine whether a point is inside or outside the interface. The following are the fundamental operations

performed on implicit functions [7],

2.3 Gradient

The gradient of an implicit function ϕ is defined as

$$\bigtriangledown\phi = \left(\frac{\partial\phi}{\partial x}, \frac{\partial\phi}{\partial y}, \frac{\partial\phi}{\partial z}\right) \tag{2.1}$$

The gradient $\bigtriangledown\phi$ is a vector quantity and its direction at any point in ϕ is perpendicular to the iso-contours of ϕ, in the direction of increasing ϕ. The unit vector outwardly normal at any point in ϕ is given by the mathematical expression

$$\widehat{N} = \frac{\bigtriangledown\phi}{\mid \bigtriangledown\phi \mid} \tag{2.2}$$

2.4 Heaviside Step function

At times we need to calculate only on the values that are inside and outside the zero level of ϕ. This function allows us to do so and is defined as

$$H(\phi) = \begin{cases} 0 & \text{if} \quad \phi < 0 \\ 1 & \text{if} \quad \phi \geqslant 0 \end{cases} \tag{2.3}$$

ϕ multiplied with $H(\phi)$ gives those values of ϕ which are within the zero level isocontour of ϕ. To obtain the values which are outside, we multiply ϕ with $(1 - H(\phi))$. From the mathematical implementation point of view, Heaviside function is given by the following expression

$$H(\phi) = \begin{cases} 0 & \text{if} \quad \phi < -\varepsilon \\ \frac{1}{2} + \frac{\phi}{2\varepsilon} + \frac{1}{2\pi}\sin\left(\frac{\pi\phi}{\varepsilon}\right) & \text{if} \quad -\varepsilon \leqslant \phi \leqslant \varepsilon \\ 1 & \text{if} \quad \phi > \varepsilon \end{cases} \tag{2.4}$$

where, ε is a parameter of very small magnitude.

2.5 Dirac delta function

Dirac delta function is the directional derivative of the Heaviside function $H(\cdot)$ in the normal direction $\widehat{N}$.

$$\delta(\overrightarrow{x}) = \bigtriangledown H(\phi(\overrightarrow{x})).\widehat{N} \tag{2.5}$$

where, $\overrightarrow{x}$ is a multidimensional variable. The delta function $\delta(\cdot)$ is identically zero everywhere except $\phi = 0$. This function is implemented using the following equation 2.6

$$\delta(\phi) = \begin{cases} \frac{1}{2\varepsilon} + \frac{1}{2\varepsilon}\cos\left(\frac{\pi\phi}{\varepsilon}\right) & \text{if} -\varepsilon \leqslant \phi \leqslant \varepsilon \\ 0 & \text{for other values of} \quad \varepsilon \end{cases} \tag{2.6}$$

As evident, the above equation 2.6 is simply a derivative of 2.4.

2.6 Signed Distance Function

Let $\partial\Omega$ be a boundary of a curve or surface defined in the domain Ω. A distance function $d(\overrightarrow{x})$ is defined by the following expression

$$d(\overrightarrow{x}) = \min(\mid x - x_I \mid) \qquad \text{for all} \qquad x_I \in \partial\Omega \tag{2.7}$$

This means that distance function gives us the shortest path or the line of sight distance of a point in the domain from the interface. In other words, distance function gives us the steepest descent between the point and interface. As a consequence of this, we have $d(\overrightarrow{x}_I) = 0$ as the point itself lies on the boundary. $d(\cdot)$ is the Euclidean distance, so we have $\mid \bigtriangledown d \mid = 1$.

A signed distance function is an implicit function ϕ such that $\mid \phi(x) \mid = d(\overrightarrow{x})$ for all values of $\overrightarrow{x}$ and $\phi(x) = +d(\overrightarrow{x})$ when $\overrightarrow{x}$ is enclosed within ϕ and $\phi(x) = -d(\overrightarrow{x})$ when $\overrightarrow{x}$ is outside ϕ.

2.7 Basic Implementation

Let us assume a shape boundary in two dimension is a closed curve Γ. This closed curve is represented as the zero-level set of a higher dimensional auxiliary function ϕ. Mathematically, we can write,

$$\Gamma = \{(x, y) \mid \phi(x, y) = 0\} \tag{2.8}$$

The level-set method operates on Γ *implicitly* through the function ϕ. Say, if the curve Γ moves in the normal direction with velocity v, then the level set function ϕ satisfies the level set equation 2.9.

$$\frac{\partial\phi}{\partial t} = v \mid \bigtriangledown\phi \mid . \tag{2.9}$$

Here, $\mid \cdot \mid$ is the Euclidean norm and t is time. This is a PDE which can be solved numerically, for example, by using finite differences on a Cartesian grid [7].

Reference

[1] B. Jahne and H. Haubecker, 2000. Computer vision and applications. A Guide for Students and Practitioners.

[2] R. M. Haralick and L. G. Shapiro, 1992. Computer and robot vision (Vol. 1, pp. 28-48). Reading: Addison-wesley.

[3] M. Kass, A. Witkin and D. Terzopoulos, 1988. Snakes: Active contour models. International journal of computer vision, 1(4), pp.321-331.

[4] C. Xu and J. L. Prince, 1998. Snakes, shapes, and gradient vector flow. IEEE Transactions on image processing, 7(3), pp.359-369.

[5] S. Osher and R. Fedkiw, 2006. Level set methods and dynamic implicit surfaces (Vol. 153). Springer Science and Business Media.

[6] H. K. Zhao, S. Osher and R. Fedkiw, 2001. Fast surface reconstruction using the level set method. In Proceedings IEEE Workshop on Variational and Level Set Methods in Computer Vision (pp. 194-201). IEEE.

[7] J. A. Sethian, 1999. Level set methods and fast marching methods: evolving interfaces in computational geometry, fluid mechanics, computer vision, and materials science (Vol. 3). Cambridge university press.

[8] A. Fenster and B. Chiu, 2006, January. Evaluation of segmentation algorithms for medical imaging. In 2005 IEEE Engineering in Medicine and Biology 27th Annual Conference (pp. 7186-7189). IEEE.

Chapter 3

LITERATURE REVIEW AND CONTRIBUTION

In this chapter, we would look into the existing methods for segmentation of medical images. This chapter is divided into 3 sections, corresponding to three category of medical images segmentation, namely lung nodule, brain tumour and cell image. The various approaches proposed in literature are discussed as follows.

3.1 Lung Nodule Segmentation

Lung nodule segmentation is a popular research area and quite a number of works exist in this area. This section is again categorized into two parts

- Non-learning based methods
- Learning based methods

3.1.1 Non-learning based methods

Zhao et al. [1] proposed a nodule segmentation algorithm on helical CT scan images based on density threshold, gradient strength and shape constraint of the nodule. However, this algorithm cannot segment nodules attached to pleural surface of the lung due to similar intensities. A semi-automatic lung nodule segmentation approach was proposed by Diciotti et al. [2] which uses the knowledge of the radiologists in a reproducible way. The main disadvantage of this method is that it requires considerable interactions and interference from the user. Dehmeshki et al. [3] presented a pulmonary nodule segmentation algorithm for nodules with a vascular and pleural attachment. This method is highly dependent on user input and requires a huge number of parameters. Failing to tune these parameters will change the segmentation result. Tachibana et al. [4] proposed a lung nodule segmentation method based on multiple thresholds and template matching. Their method sometimes result in poor accuracy and low efficiency because of complex space transformation and dynamic programming. Kishore et al. [5] performed lung nodule detection by combining watershed transform and morphological region segmentation. Li et al. [6] proposed a selective nodule enhancement filter to enhance the nodule shape and structure by dominating the presence of other anatomical structures in the lung region. Goncalves et al. [7] proposed a multi-scale segmentation strategy that uses the central medialness adaptive principle, a Hessian-based strategy that was originally formulated for tubular extraction. Jung et al. [8] formulated a ground-glass nodule segmentation method that can separate solid component and ground glass opacity (GGO) using an asymmetric multi-phase deformable model in chest CT images. Initial solid component and GGO were first extracted using intensity-based segmentation with histogram modeling and then the initial extracted regions were refined using an asymmetric multi-phase deformable method with modified energy functional and intensity-constrained averaging function. Finally, vessel-like structures are removed using multi-scale shape analysis.

Level sets have also been employed for lung nodule segmentation. Swierczynski et al. [9] presented a methodology for joint image segmentation and registration in lung CT images using

level sets. Farag et al. [10] proposed a variational level set approach for lung nodule segmentation, where a circular model is a shape prior, which is integrated as a signed distance function. This method can overcome the problem of nodules attached to the lung walls and vessels.

3.1.2 Learning based methods

Here, we are going to mention few works that used deep learning for nodule segmentation. A hybrid system for lung nodule segmentation was proposed by Messay et al. [11] where a model based technique was combined with a trained neural network for segmentation. Here the solution is semiautomatic, and the performance of the algorithm degrades with a decrease in user interventions. In recent research works, powerful supervised techniques like deep convolutional neural networks are often integrated with traditional model based segmentation approaches. For example, Mukherjee et al. [12] proposed a novel solution for lung nodule segmentation using deep learned prior based graph cut. The method obtains information of the location of the object using deep learning and the graph cut method is used to preserve the morphological intricacies of the objects. Similarly, Roy et al. [13] proposed a synergism of deep learning and shape driven level sets for automated and accurate lung nodule segmentation. A coarse-to-fine solution was adopted, where, at first, a deep fully convolutional network was employed to obtain coarse segmentation and then a shape driven level set to achieve fine segmentation. Wang et al. [14] proposed a data-driven model, termed as Central Focused Convolutional Neural Networks (CF-CNN), for segmenting lung nodules from heterogeneous CT images. The proposed model captured a diverse set of nodule-sensitive features from both 2-D and 3-D CT images simultaneously. While classifying an image voxel, the effect of its neighbor voxels vary according to their spatial locations. This effect was observed because of a novel central pooling layer that retained much information on voxel patch center.

3.2 Brain Tumour Segmentation

A variety of methods have been proposed in literature for brain tumour segmentation. The methods employed to perform brain tumour segmentation include thresholding and morphological techniques, watershed method, region growing approach, asymmetry analysis, atlas-based method, contour/surface evolution method, interactive algorithm, and supervised and unsupervised learning methods. However, similar to the above section 3.1, we are categorizing the methods broadly into non-learning and learning based.

3.2.1 Non-learning based methods

Low-level operations, like thresholding, edge detection, and morphological techniques are fast and can be easily adjusted [15]. Biji et al. [16] employed two segmentation schemes namely Modified Fuzzy thresholding and Modified minimum error thresholding for segmentation of brain tumours. Gibbs et al. [17] proposed a segmentation method based on morphological edge detection and region growing. However, the tumour segmentation performance of these methods are highly dependent on evident difference in the intensities between tumour and non-tumour regions. Watershed and region growing techniques are simple and consistently produce complete boundaries [18]. Hsieh et al. [19] proposed an algorithm integrating fuzzy-c-mean (FCM) and region growing method for automated tumour image segmentation. However, these two techniques are sensitive to noise, which is a common problem in any intensity-based methods. Moreover, many intensity-based methods tend to over-segment tumours because of the weak and diffused edges caused by edema.

A healthy human brain is symmetric about the mid-sagittal plane. The asymmetric analysis method proposed by Saha et al. [20] and Iscan et al. [21] for tumour segmentation is based on the principle that tumours, which appear in one of the cerebral hemispheres, can cause asymmetry between the left and right cerebral hemispheres. However, asymmetry analysis might not be useful when a tumour is located across the mid-sagittal plane.

Brain atlases can provide important data, prior to tumour segmentation enhancement by measuring the difference between normal and abnormal brain structure. Atlas-based segmentation methods have been investigated in [22], [23] and [24]. For instance, Iglesias et al. [22] proposed a generative probabilistic method for solving the atlas-to-target registrations and label fusion steps simultaneously. This model does not directly rely on the similarity of image intensities. Gooya et al. [24] proposed to modify a healthy atlas by using tumour growth models and to perform a joint segmentation and registration to a modified brain atlas. Similarly, Prastawa et al. [25] proposed a tumour segmentation method that is guided by differences between the patient scan and the atlas of healthy brain. One limitation of this approach is the fact that it ignores the mass effect (deformation of neighboring healthy structures) caused by the tumour, which can lead to incorrect registration. The problem with these methods are that deformable registration of the brain atlas to brain images with tumour is an extremely challenging task because of the intensity variations around the tumour caused by edema and the deformations of healthy tissue morphology caused by the tumour mass effect [26].

The contour or surface evolution method has been widely used for the tumour segmentation of 2-D and 3-D data in [27]–[29]. Sachdeva et al. [27] proposed content-based active contour (CBAC) that uses both intensity and texture information present within the active contour. In Taheri et al. [28] proposed methodology, the level set speed function is designed using a global threshold. This threshold is defined based on the idea of confidence interval and is iteratively updated throughout the evolution process. Wang et al. [29] proposed a new approach called the Fluid Vector Flow (FVF) active contour model to address problems like insufficient capture range and poor convergence. However, these contour and surface evolution methods are not independent of the initialization process.

Graph-based segmentation framework is a popular method among interactive algorithms for image segmentation. Jiang et al. [30] proposed graph-based seeded segmentation as a global optimization approach. As this method needs manual seed selection for different tissues, the procedure may not include all tumour areas within the volume of interest along the depth direction, thus leading to tumour under segmentation.

In many works, unsupervised learning method, such as k-means and fuzzy clustering, have been used for brain tumour segmentation. Supervised classification learning method approaches have also been used, as they can extract discriminative information from the training data by using well-trained classifiers for tumour segmentation. Some of such approaches are discussed. Bauer et al. [31] used Support Vector Machine (SVM) as voxelwise classifiers for developing discriminative models to segment brain tumours. Geremia et al. [32] proposed a model that classify each voxel of a multimodal MR brain image by random forest, using features capturing information from neighbouring voxels and from distant regions such as the symmetric part of the brain. More recently, Le Folgoc et al. [33] proposed Lifted Auto-Context Forests, an efficient method based on cascaded Random Forests which progressively segment tumour sub-classes.

3.2.2 Learning based methods

In recent years, Convolutional Neural Networks achieved significant results in many tasks of brain tumour segmentation [34]. In particular, the representation learning ability of CNNs is a considerable advantage for the task of tumour segmentation, where the design of discriminant image features are nontrivial. Pereira et al. [35] proposed a methodology to segment brain

tumours using a Deep Convolutional Neural Network. Their work focused on the fact that Neural Networks suffer from overfitting. To address it they used Dropout, Leaky Rectifier Linear Units and small convolutional kernels. They also used two different architectures and trained them to segment the High Grade and Low Grade Gliomas respectively. Ronneberger et al. [36] proposed a network and training strategy that relies on the strong use of data augmentation to use the available annotated samples more efficiently. Their architecture consists of a contracting path to capture context and a symmetric expanding path that enables precise localization. Moreover, such a network can be trained end-to-end. Havaei et al. [37] proposed a novel CNN architecture which exploits both local features as well as global contextual features simultaneously. A unique element of their network is the use a final layer that is a convolutional implementation of a fully connected layer, which allows a 40 fold speed up. Also they proposed a 2-phase training procedure that allows us to tackle difficulties related to the imbalance of tumour labels. Zheng et al. [38] proposed a method based on deep learning to perform cardiac segmentation on short axis MR imaging stacks iteratively from the top slice (around the base) to the bottom slice(around the apex). At each iteration, a novel variant of the U-net is applied to propagate the segmentation of a slice to the adjacent slice below it. In other words, the prediction of a segmentation of a slice is dependent upon the already existing segmentation of its adjacent slice. Dou et al. [39] proposed a novel and efficient 3D fully convolutional network equipped with a 3D deep supervision mechanism (DSN) to comprehensively address challenges like optimization difficulties of 3D networks and inadequacy of training samples. The proposed 3D DSN is capable of conducting volume-to-volume learning and inference, which can eliminate redundant computations and alleviate the risk of over-fitting on limited training data. More importantly, the 3D deep supervision mechanism can effectively cope with the optimization problem of gradients vanishing or exploding when training a 3D deep model, accelerating the convergence speed and simultaneously improving the discrimination capability. Such a mechanism was developed by deriving an objective function that directly guides the training of both lower and upper layers in the network, so that the adverse effects of unstable gradient changes can be counteracted during the training procedure. They also employed a fully connected conditional random field model as a post-processing step to refine the segmentation results. Wang et al. [40] proposed a cascade of fully convolutional neural networks to segment brain tumour. Their network consist of multiple layers of anisotropic and dilated convolution filters, combined with multi-view fusion to reduce the false positives.

Despite promising results obtained by deep learning methods, segmentation of brain tumours is still a very challenging task. One of the main drawbacks of CNNs is their computational cost resulting from application of thousands of costly operations (convolutions, poolings, upsamplings, downsamplings) on input images. This aspect is particularly problematic for segmentation problems in large medical images such as MRI or CT scans. Despite the variety of proposed neural network architectures, current CNN-based systems struggle to capture a large 3D context from input images. Moreover, most methods implicitly assume the presence of all MR sequences for all patients and the correct registration between sequences whereas these conditions do not necessarily hold in reality always.

3.3 Cell Segmentation

Many methods for the segmentation of cells have been proposed in literature. The approaches can be broadly grouped into three classes: i) Thresholding and morphological operations ii) Watershed transformation iii) Machine learning

The approaches in the first category are based on Thresholding and the combinations of some morphological operations [41],[42]. The method in [41] uses morphological operators to initialize a level set function that is iteratively evolved till the convergence of the zero level set takes place

to the cell boundary. Similarly, the method in [42] implements an iterative approach based on morphological operations, where the authors have proposed an iterative erosion method based on information about gray level and gradient intensity. Though this method works for different types of cell images, it suffers from a high number of false seeds as noise blobs might be detected as real cells. The approach in [43] tries to address this problem by implementing a multi-thresholding operation controlled by means of a rule-based verification procedure, such that each segmented blob is considered as a cell on the basis of information like area size, shape and position. This approach was tested only on four common antinuclear antibody (ANA) patterns, namely speckled, homogeneous, centromere and nucleolar while difficult staining patterns like nuclear membrane, golgi and mitotic spindle was not considered. In general, methods based on global thresholding followed by morphological operations face problems with cells characterized by irregular patterns. Thus, new methodologies like those proposed in [44] and [45] try to overcome this problem by differentiating the segmentation process into two or more branches according to the appearance of the regions. Unfortunately, these methods also generally provide a less accurate detection when cells include both bright and dark pixels like the centromere and the cytoplasmic.

The method proposed by Hodneland et al. [46] tries to address this limitation by exploiting a PDE watershed that requires no pre-defined markers and provides a simultaneous regularization of the watershed contours. However, the methods belonging to this second category that are based on watershedding algorithms, like the HodnelandâĂŹs approach, generally suffer from over-segmentation issue. Tonti et al. [47] address this problem by introducing an automatic process to select seeds according to the nature and characteristics of the input image. Unfortunately, this method still needs to be extended to segment some kinds of cells, such as cytoplasmic cells.

As we have seen, several methods in the first two categories are not able to deal with some kinds of difficult images, such as the centromere cells and the cytoplasmic cells.

Therefore, methods in the third category aim to generalize to a wider range of images by adopting supervised techniques. They are based on machine learning techniques and deal with the high variability of biological images by training classifiers on labeled images. For example, in [48] three different classes of pixels are generated on the basis of the gray scale values of the pixels. Pixels with the lowest and highest gray scale value or intensity are easily associated with the background and the foreground respectively, while the medium-intensity ones are handled by the learning process which uses a dilation operation to aggregate patches of non-marked pixels. Another approach that combines deep CNN with multiple instance learning to segment and classify microscopy images has been proposed in [49]. In [50], the authors have proposed a supervised kernel based fuzzy c-means clustering, that exploits the level set method presented in [51] and a Bayes classifier to assign class memberships to each pixel of an image. The method proposed by Prasath et al. [52] also implements a classification approach at pixel level, by adopting Random Forest classifiers. As confirmed by the results obtained, machine learning based approaches are affected by an under-segmentation that is generally caused by the small dimensions of the training dataset that cause overfitting. An accurate foreground detection of biological images is important, as it represents a preliminary step for the separation and counting of the cells in the image. Indeed, cell counting is a crucial task in the diagnosis of various diseases such as anemia, leukemia, and coronary heart diseases. A technique based on circular Hough transform and thresholding has been presented in [53] to count blood cells. But, often cells either show an irregular shape or are grouped in clusters impeding the capability of the Hough transform to detect objects that deviate significantly from the circular form. This limitation also affects other approaches in the literature that rely on the idea of detecting only circular shapes in the image, even if by means of different techniques like those presented by Kofahi et al. [54] and Stegmaier et al. [55]. Both these methods depend on LoG filters that are generated from rotational symmetric Gaussian kernels and encounter problems in detecting blobs with general elliptical structure. However, the approach introduced by Khan and Maruf [56] overcame this

limitation by implementing a pattern matching based on the distance transform map. Though this approach outperforms the state of the art methods in terms of accuracy, it generally tends to undercount the number of cells, showing a high number of false negatives.

3.4 Contribution

In this work, we propose a level set based segmentation technique by taking into consideration the challenges involved in medical image segmentation like low contrast images, irregular shapes, lesion attached with similar intensity structures etc. We choose a classical segmentation tool namely level set method as it is less computationally expensive unlike deep learning network. Also, deep network requires a huge training data and ground truth which may not be available all the time in medical imaging applications. Existing level set methods are sensitive to initialization and give poor performance in case of low contrast images. Considering these drawbacks, we improve the existing level set method by modifying the initialization of level set and incorporating the contrast and shape information into the existing framework. Now, we highlight the contributions:

1. **Robust initial level set function**: A modified initial level set function is proposed which is robust in nature, *i.e.*, the contour evolution of the proposed level set does not depend on the position of initialization. We are using three types of initial level set functions to prioritize the nature of the image to be segmented. A constant level set function gives equal priority to all the regions having same intensity and has a fixed value for every index or co-ordinate across the image domain. A step level set function is used for multiple region segmentation and it has two different values, one within and the other outside the region to be segmented. The step level set function also gives equal priority to the region inside and outside the initial level set which results in false segmentation as well. A Gaussian level set initialization is introduced which gives higher priority only to the lesion/region to be segmented which in turn reduces the false segmentation.

2. **Intensity and shape driven level set**: An intensity and shape driven level set evolution algorithm is introduced. It mines the intensity and shape information of the image to be segmented in an automated fashion and sets the parameters of the level set. The intensity term is incorporated to handle the segmentation of low-contrast images and it also helps in the segmentation of multiple regions having similar intensity. A weight factor is introduced in the area term of level set method based on the circularity of the evolving contour to prioritize the circular and non-circular region to be segmented. This in turn provides accurate segmentation of different types of medical images depending on the shape of the lesion.

Reference

[1] B. Zhao, D. Yankelevitz, A. Reeves and C. Henschke, 1999. Two –dimensional multi –criterion segmentation of pulmonary nodules on helical CT images. Medical Physics, 26(6), pp.889-895.

[2] S. Diciotti, G. Picozzi, M. Falchini, M. Mascalchi, N. Villari and G. Valli, 2008. 3-D segmentation algorithm of small lung nodules in spiral CT images. IEEE Transactions on Information Technology in Biomedicine, 12(1), pp.7-19.

[3] J. Dehmeshki, H. Amin, M. Valdivieso and X. Ye, 2008. Segmentation of pulmonary nodules in thoracic CT scans: a region growing approach. IEEE transactions on medical imaging, 27(4), pp.467-480.

[4] R. Tachibana and S. Kido, 2006, March. Automatic segmentation of pulmonary nodules on CT images by use of NCI lung image database consortium. In Medical Imaging 2006: Image Processing (Vol. 6144, p. 61440M). International Society for Optics and Photonics.

[5] V. V. Kishore and R. V. S. Satyanarayana, 2013, February. Performance evaluation of edge detectors-morphology based ROI segmentation and nodule detection from DICOM lung images in the noisy environment. In 2013 3rd IEEE International Advance Computing Conference (IACC) (pp. 1131-1137). IEEE.

[6] Q. Li, F. Li and K. Doi, 2008. Computerized detection of lung nodules in thin-section CT images by use of selective enhancement filters and an automated rule-based classifier. Academic radiology, 15(2), pp.165-175.

[7] L. Goncalves, J. Novo and A. Campilho, 2016. Hessian based approaches for 3D lung nodule segmentation. Expert Systems with Applications, 61, pp.1-15.

[8] J. Jung, H. Hong and J. M. Goo, 2018. Ground-glass nodule segmentation in chest CT images using asymmetric multi-phase deformable model and pulmonary vessel removal. Computers in biology and medicine, 92, pp.128-138.

[9] P. Swierczynski, B. W. PapieÅij, J. A. Schnabel, and C. Macdonald, 2018. A level-set approach to joint image segmentation and registration with application to CT lung imaging. Computerized Medical Imaging and Graphics, 65, pp.58-68.

[10] A. A. Farag, H. E. A. El Munim, J. H. Graham, 2013. A novel approach for lung nodules segmentation in chest CT using level sets. IEEE Transactions on Image Processing, 22(12), pp.5202-5213.

[11] T. Messay, R. C. Hardie and T. R. Tuinstra, 2015. Segmentation of pulmonary nodules in computed tomography using a regression neural network approach and its application to the lung image database consortium and image database resource initiative dataset. Medical image analysis, 22(1), pp.48-62.

[12] S. Mukherjee, X. Huang, R.R. Bhagalia, Lung nodule segmentation using deep learned prior based graph cut, in: Biomedical Imaging (ISBI 2017), 2017 IEEE 14th International Symposium on, IEEE, 2017, pp. 1205âĂŞ1208.

[13] R. Roy, T. Chakraborti and A. S. Chowdhury, 2019. A Deep Learning-Shape Driven Level Set Synergism for Pulmonary Nodule Segmentation. Pattern Recognition Letters.

[14] S. Wang, M. Zhou, Z. Liu, Z. Liu, D. Gu, Y. Zang, D. Dong, O. Gevaert and J. Tian, 2017. Central focused convolutional neural networks: Developing a data-driven model for lung nodule segmentation. Medical image analysis, 40, pp.172-183.

[15] D. Bhattacharyya and T. H. Kim, 2011, April. Brain tumour detection using MRI image analysis. In International Conference on Ubiquitous Computing and Multimedia Applications (pp. 307-314). Springer, Berlin, Heidelberg.

[16] C. L. Biji, D. Selvathi and A. Panicker, 2011, July. tumour detection in brain magnetic resonance images using modified thresholding techniques. In International Conference on Advances in Computing and Communications (pp. 300-308). Springer, Berlin, Heidelberg.

[17] P. Gibbs, D. L. Buckley, S. J. Blackband and A. Horsman, 1996. Tumour volume determination from MR images by morphological segmentation. Physics in Medicine and Biology, 41(11), p.2437.

[18] R. Ratan, S. Sharma and S. K. Sharma, 2009. Brain tumour detection based on multiparameter MRI image analysis. ICGST-GVIP Journal, 9(3), pp.9-17.

[19] T. M. Hsieh, Y. M. Liu, C. C. Liao, F. Xiao, I. J. Chiang and J. M. Wong, 2011. Automatic segmentation of meningioma from non-contrasted brain MRI integrating fuzzy clustering and region growing. BMC medical informatics and decision making, 11(1), p.54.

[20] B. N. Saha, N. Ray, R. Greiner, A. Murtha and H. Zhang, 2012. Quick detection of brain tumours and edemas: A bounding box method using symmetry. Computerized medical imaging and graphics, 36(2), pp.95-107.

[21] Z. Iscan, Z. Dokur and T. Olmez, 2010. tumour detection by using Zernike moments on segmented magnetic resonance brain images. Expert Systems with Applications, 37(3), pp.2540-2549.

[22] J. E. Iglesias, M. R. Sabuncu and K. Van Leemput, 2013. A unified framework for cross-modality multi-atlas segmentation of brain MRI. Medical image analysis, 17(8), pp.1181-1191.

[23] H. Wang, J. W. Suh, S. R. Das, J. B. Pluta, C. Craige and P. A. Yushkevich, 2013. Multi-atlas segmentation with joint label fusion. IEEE transactions on pattern analysis and machine intelligence, 35(3), pp.611-623.

[24] A. Gooya, K. M. Pohl, M. Bilello, L. Cirillo, G. Biros, E. R. Melhem and C. Davatzikos, 2012. GLISTR: glioma image segmentation and registration. IEEE transactions on medical imaging, 31(10), pp.1941-1954.

[25] M. Prastawa, E. Bullitt, S. Ho and G. Gerig, 2004. A brain tumour segmentation framework based on outlier detection. Medical image analysis, 8(3), pp.275-283.

[26] A. Gooya, G. Biros and C. Davatzikos, 2011. Deformable registration of glioma images using EM algorithm and diffusion reaction modeling. IEEE transactions on medical imaging, 30(2), pp.375-390.

[27] J. Sachdeva, V. Kumar, I. Gupta, N. Khandelwal and C. K. Ahuja, 2012. A novel content-based active contour model for brain tumour segmentation. Magnetic resonance imaging, 30(5), pp.694-715.

[28] S. Taheri, S. H. Ong and V. F. H. Chong, 2010. Level-set segmentation of brain tumours using a threshold-based speed function. Image and Vision Computing, 28(1), pp.26-37.

[29] T. Wang, I. Cheng and A. Basu, 2009. Fluid vector flow and applications in brain tumour segmentation. IEEE Transactions on Biomedical Engineering, 56(3), pp.781-789.

[30] J. Jiang, Y. Wu, M. Huang, W. Yang, W. Chen and Q. Feng, 2013. 3D brain tumour segmentation in multimodal MR images based on learning population-and patient-specific feature sets. Computerized Medical Imaging and Graphics, 37(7-8), pp.512-521.

[31] S. Bauer, L. P. Nolte and M. Reyes, 2011, September. Fully automatic segmentation of brain tumour images using support vector machine classification in combination with hierarchical conditional random field regularization. In international conference on medical image computing and computer-assisted intervention (pp. 354-361). Springer, Berlin, Heidelberg.

[32] E. Geremia, B. H. Menze and N. Ayache, 2012. Spatial decision forests for glioma segmentation in multi-channel MR images. MICCAI Challenge on Multimodal Brain tumour Segmentation, 34.

[33] L. Le Folgoc, A. V. Nori, S. Ancha and A. Criminisi, 2016, October. Lifted auto-context forests for brain tumour segmentation. In International Workshop on Brainlesion: Glioma, Multiple Sclerosis, Stroke and Traumatic Brain Injuries (pp. 171-183). Springer, Cham.

[34]: J. Long, E. Shelhamer and T. Darrell, 2015. Fully convolutional networks for semantic segmentation. In Proceedings of the IEEE conference on computer vision and pattern recognition (pp. 3431-3440).

[35]: S. Pereira, A. Pinto, V. Alves and, C. A. Silva, 2015, October. Deep convolutional neural networks for the segmentation of gliomas in multi-sequence MRI. In BrainLes 2015 (pp. 131-143). Springer, Cham.

[36] O. Ronneberger, P. Fischer and T. Brox, 2015, October. U-net: Convolutional networks for biomedical image segmentation. In International Conference on Medical image computing and computer-assisted intervention (pp. 234-241). Springer, Cham.

[37] M. Havaei, A. Davy, D. Warde-Farley, A. Biard, A. Courville, Y. Bengio, C. Pal, P. M. Jodoin and H. Larochelle, 2017. Brain tumour segmentation with deep neural networks. Medical image analysis, 35, pp.18-31.

[38] Q. Zheng, H. Delingette, N. Duchateau and N. Ayache, 2018. 3-D Consistent and Robust Segmentation of Cardiac Images by Deep Learning With Spatial Propagation. IEEE transactions on medical imaging, 37(9), pp.2137-2148.

[39] Q. Dou, L. Yu, H. Chen, Y. Jin, X. Yang, J. Qin and P. A. Heng, 2017. 3D deeply supervised network for automated segmentation of volumetric medical images. Medical image analysis, 41, pp.40-54.

[40] G. Wang, W. Li, S. Ourselin and T. Vercauteren, 2017, September. Automatic brain tumour segmentation using cascaded anisotropic convolutional neural networks. In International MICCAI Brainlesion Workshop (pp. 178-190). Springer, Cham.

[41]: A. D. Khamael, J. Banks, I. Tomeo-Reyes and V. Chandran, 2016, December. Automatic segmentation of HEp-2 cell Fluorescence microscope images using level set method via geometric

active contours. In 2016 23rd International Conference on Pattern Recognition (ICPR) (pp. 81-83). IEEE.

[42]: Z. Wang, 2016. A new approach for segmentation and quantification of cells or nanoparticles. IEEE Transactions on Industrial Informatics, 12(3), pp.962-971.

[43]: X. Jiang, G. Percannella and M. Vento, 2015, September. A verification-based multithreshold probing approach to HEp-2 cell segmentation. In International Conference on Computer Analysis of Images and Patterns (pp. 266-276). Springer, Cham.

[44]: C. C. Cheng, T. Y. Hsieh, J. S. Taur and Y. F. Chen, 2013. An automatic segmentation and classification framework for anti-nuclear antibody images. Biomedical engineering online, 12(1), p.S5.

[45]: B. Divya, H. Nanjundaswamy and N. Muniraj, 2012. Segmentatation of IIF HEp-2 ANA cells based on thresholding and connectivity. Int. J. Microsyst. Technol. Appl, 1(1), pp.26-30.

[46]: E. Hodneland, X. C. Tai and H. Kalisch, 2016. PDE based algorithms for smooth watersheds. IEEE transactions on medical imaging, 35(4), pp.957-966.

[47]: S. Tonti, S. Di Cataldo, A. Bottino and E. Ficarra, 2015. An automated approach to the segmentation of HEp-2 cells for the indirect immunofluorescence ANA test. Computerized Medical Imaging and Graphics, 40, pp.62-69.

[48]: G. Percannella, P. Soda and M. Vento, 2012, June. A classification-based approach to segment HEp-2 cells. In 2012 25th IEEE International Symposium on Computer-Based Medical Systems (CBMS) (pp. 1-5). IEEE.

[49]: O. Z. Kraus, J. L. Ba and B. J. Frey, 2016. Classifying and segmenting microscopy images with deep multiple instance learning. Bioinformatics, 32(12), pp.i52-i59.

[50]: A. Gharipour and A. W. C. Liew, 2013, July. Colon cell image segmentation based on level set and kernel-based fuzzy clustering. In International Conference on Intelligent Computing (pp. 120-129). Springer, Berlin, Heidelberg.

[51]: T. F. Chan and L. A. Vese, 2001. Active contours without edges. IEEE Transactions on image processing, 10(2), pp.266-277.

[52]: V. S. Prasath, Y. M. Kassim, Z. A. Oraibi, J. B. Guiriec, A. Hafiane, G. Seetharaman and K. Palaniappan, 2016, December. HEp-2 cell classification and segmentation using motif texture patterns and spatial features with random forests. In 2016 23rd International Conference on Pattern Recognition (ICPR) (pp. 90-95). IEEE.

[53]: M. Thejashwini and M. Padma, Counting of RBCs and WBCs using image processing technique, Int.J.RecentInnov.TrendsComput.Commun.,vol. 3, no. 5, pp. 2948–2953, 2014

[54]: Y. Al-Kofahi, W. Lassoued, W. Lee and B. Roysam, 2010. Improved automatic detection and segmentation of cell nuclei in histopathology images. IEEE Transactions on Biomedical Engineering, 57(4), pp.841-852.

[55]: J. Stegmaier, J. C. Otte, A. Kobitski, A. Bartschat, A. Garcia, G. U. Nienhaus, U. StrÃď hle and R. Mikut, 2014. Fast segmentation of stained nuclei in terabyte-scale, time resolved 3D microscopy image stacks. PloS one, 9(2), p.e90036.

[56]: H. A. Khan and G. M. Maruf, 2013, May. Counting clustered cells using distance mapping. In 2013 International Conference on Informatics, Electronics and Vision (ICIEV) (pp. 1-6). IEEE.

Chapter 4

PROPOSED METHOD

This chapter deals with the proposed methodology for segmentation of medical images. In our proposed method, we propose a intensity and shape driven level set where the initial level set is robust in nature *i.e.*, the contour evolution of the proposed level set does not depend on the position of initialization.

4.1 Introduction to level set function

The evolution of our level set function is governed by the PDE given in equation (4.1). The governing equation is :

$$\frac{\partial \phi}{\partial t} = \alpha F_{adf} + \beta F_{svf} + \zeta R_{dr} + \nu R_{vr} \tag{4.1}$$

From the above equation, the factors which are controlling the evolution of the level set function are

- Contrast Adaptive Driving Force F_{adf}
- Shape Variation Force F_{svf}
- Distance Regularization R_{dr}
- Variance Regularization R_{vr}

The distance regularization term R_{dr} and variance regularization term R_{vr} as given by [3] and [1] respectively are used in the proposed energy function of level set evolution. The accuracy of numerical computation of the evolving LSF depends largely on the degree of stability of its evolution. This demands that the our LSF is smooth and does not become too steep or flat at least in the vicinity of the zero level contour. This condition is satisfied by a SDF by virtue of its property $|\nabla\phi|$=1. Hence, the SDF has been widely used as level set functions. In conventional formulations, the LSF is typically initialised and periodically re-initialized to maintain the signed distance property [3]. This energy functional is basically a penalty term which penalizes the deviation of the LSF from a SDF, and hence completely eliminates the need for reinitialization without hampering smmooth evolution. The Distance regularization term of equation 4.1 is mathematically given by the following expression as obtained from [3],

$$R_{dr} = div\left(d_p\left(|\nabla\phi|\right)\nabla\phi\right) \tag{4.2}$$

Image segmentation is largely affected by the presence of noise in an image. To maintain high degree of accuracy by eliminating noise while preserving the edges in an image is a challenging task. Presence of noise hampers the evolution of the level set function. To remove the noise present in the image we use the variance regularization term given by Wang et al [1] as

$$R_{vr} = g\left(|\bigtriangledown I_\sigma|\right) div\left(\frac{\bigtriangledown\phi}{|\bigtriangledown\phi|}\right) \tag{4.3}$$

The theory and mathematics involved in our key contribution areas, constant adaptive driving force F_{adf} and shape variation force F_{svf}, are discussed in the following sections.

4.2 Robust Initial Level Set function

A modified initial level set function is proposed which is robust in nature *i.e.*, the contour evolution of the proposed level set does not depend on the position of initialization. We are using three types of initial level set functions to prioritize the nature of the lesion to be segmented.

1. Constant : A function which have a fixed value for every index or coordinate in the image domain.
2. Step : A function with two different values, one within and other outside a specified region in the image domain.
3. Gaussian : A function whose values vary across the entire image domain in a Gaussian form.

The functions mentioned above are shown in the following figure 4.1

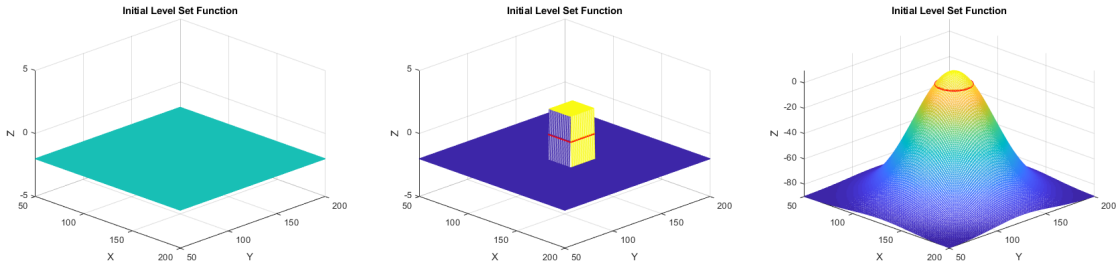

(a) Constant (b) Step (c) Gaussian

Figure 4.1: Types of initial level set function

A **Constant** initial level set function is applicable to those formulations where an initial zero level set contour is actually not required to begin the segmentation process. In our formulation, the constant level set function can be used as the *Contrast Adaptive force* term in our formulation "moulds" this function according to the intensity information in the image as a result of which the zero level contour and shape variation force (which was initially zero due to absence of zero level set), now comes into play and guides further evolution along with the intensity factor. In our method, this function is used when we need to segment multiple objects in an image. A **Step** function is normally used when we need an initial zero-level contour and at the same time have equal priority for the entire image domain. This type of function has been used in [2]-[4]. The zero level set was initialized within the object to be segmented and from there the propagation of the zero level set took place towards the edges of the object. Just as constant function, step function is used for multi-object segmentation in our proposed methodology. A **Gaussian** function is used when we need to segment a particular object in an image and avoid unwanted segmentation of regions having similar intensities. This function also have a zero level contour and the magnitude of this function is highest at the centre of this contour or the seed points from where it gradually falls off as we move away from the seed point. This implies that we are providing less priority for objects having similar intensities but are not a part of the object to be segmented. In a constant function, there are no seed points. Even in the case of a Step and Gaussian function, where there are seed points, the segmentation results are independent of their position. In case of a Step function, the contrast adaptive force term causes initial level set function to adaptively move up and down based on intensity information and shape factor of the image. In case of Gaussian function, the intensities within the object to be segmented being nearly equal, the zero level set contour tends to grow in all directions in way decided by

the shape priority until some edge is reached. Consider the following two figures. In figure 4.2 shows a Constant function, having no seed points, segment a cell image (multiple object) and figures 4.3-4.4 show that though the Gaussian function is initialised at two different positions in these two figures to segment a lung nodule (single object), they yield the same result.

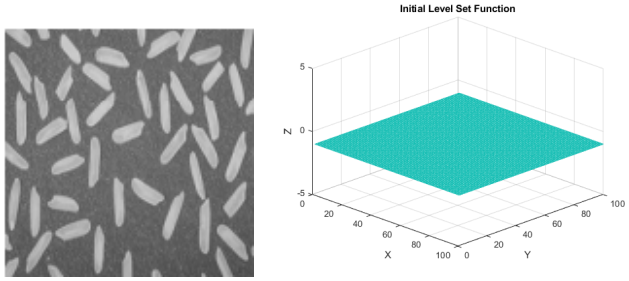

(a) Cell Image

(b) Constant function

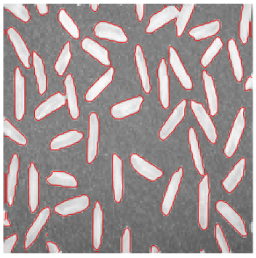

(c) Segmented Image of cell

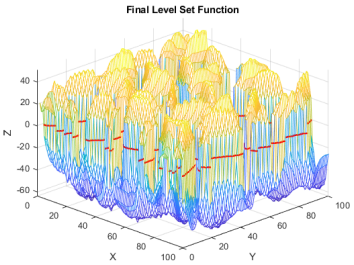

(d) Final Level set function

Figure 4.2: Cell segmentation independent of seed points

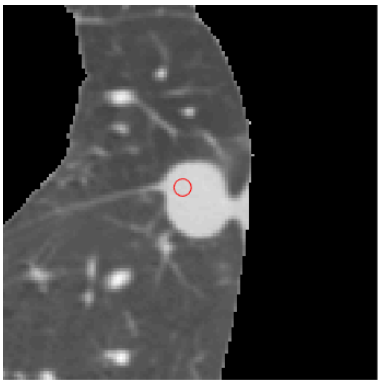

(a) Initialised randomly

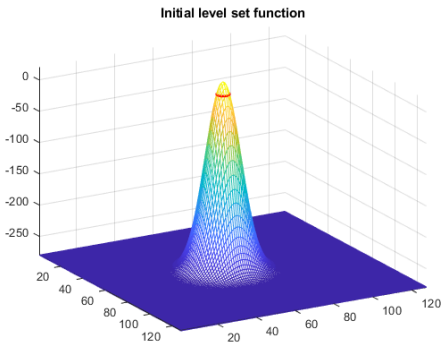

(b) Initial level set function

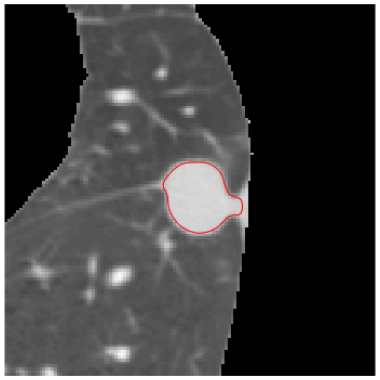

(c) Final segmented output

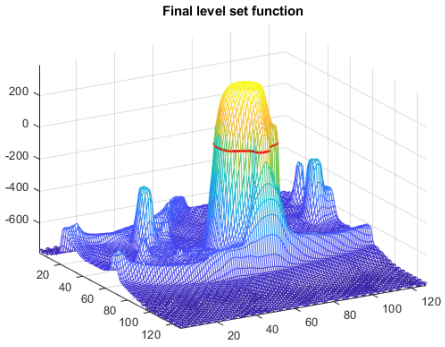

(d) Final level set function

Figure 4.3: An example showing nodule segmentation independent of initial seed points

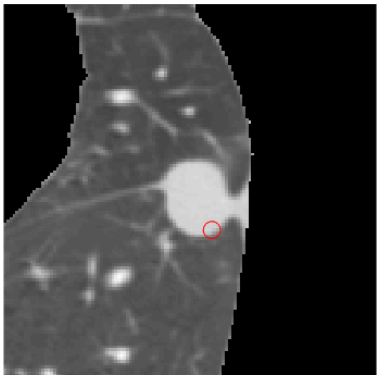

(a) Initialised randomly

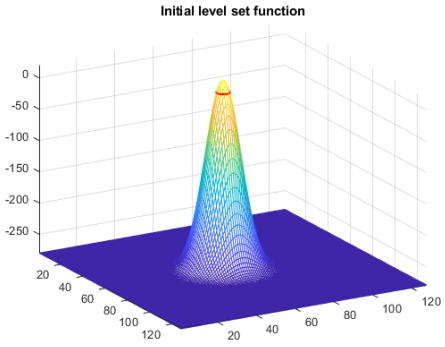

(b) Initial level set function

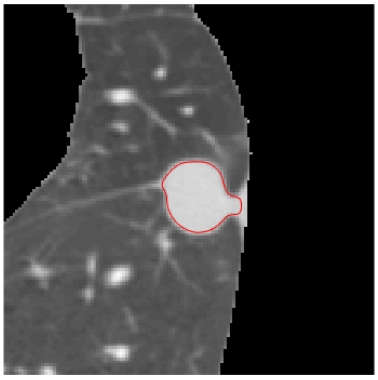

(c) Final segmented output

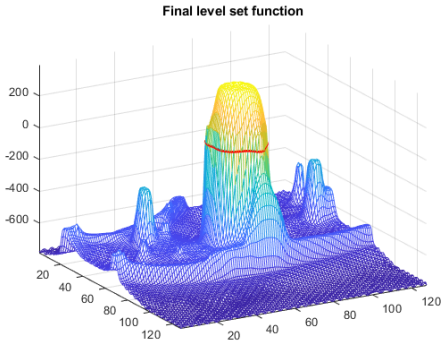

(d) Final level set function

Figure 4.4: Another example showing nodule segmentation independent of initial seed points

To segment multiple objects, we use Constant or Step function, whereas to segment single object we use Gaussian function. The following figure 4.5 show the segmentation result when a step function is used to segment lung nodule and a gaussian function is used to segment a cell image. Clearly, the obtained results are not correct showing the importance of the choice of initial level set function.

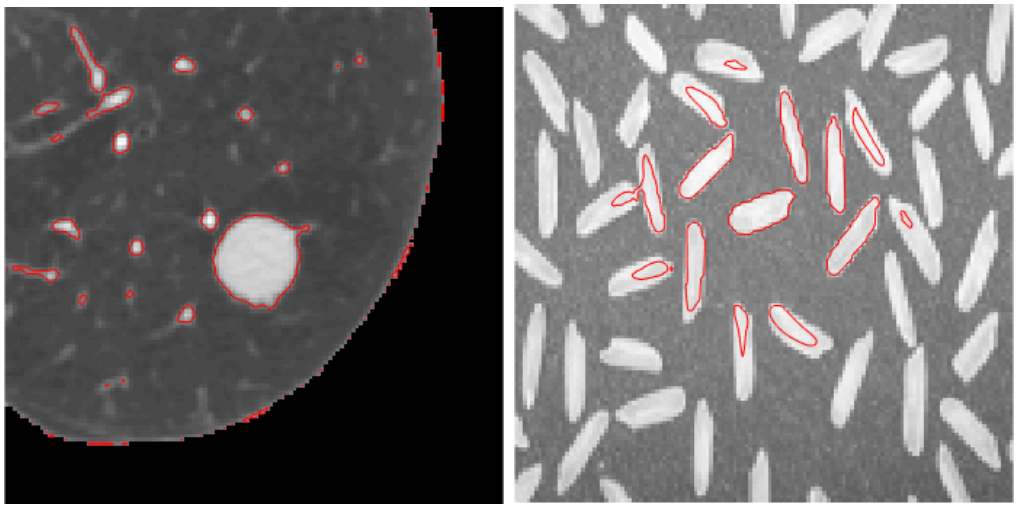

(a) Step function on a lung nodule (b) Gaussian function on a cell

Figure 4.5: Inappropriate choice of initial level set function for nodule and cell segmentation

4.3 Intensity and Shape driven level set

In this section we are going to describe the Contrast Adaptive Driving force term which works on the intensity distribution in the image and Shape Variation force term which prioritizes the nature of evolution of the level set function.

4.3.1 Contrast Adaptive Driving Force

We pursue the idea in [1] where for a given image $I : \Omega \to \mathbb{R}$ and a Lipschitz function $\phi(x, y) : \Omega \to \mathbb{R}$, given $\Omega \subset \mathbb{R}^2$ in the image domain, the contrast adaptive driving force was defined as

$$f(I, c_1, c_2) = \textit{sign}\left(I\left(x, y\right) - \frac{c_1 + c_2}{2}\right) \tag{4.4}$$

c_1 is same as that defined in [1]. We have modified c_2 to fit our purpose of medical image segmentation. c_2 as defined in [1] is

$$c_2\left(\phi\right) = \frac{\int_\Omega I\left(x, y\right) H\left(-\phi\left(x, y\right)\right) dxdy}{\int_\Omega H\left(-\phi\left(x, y\right)\right) dxdy} \tag{4.5}$$

As per the above equation, we are calculating the average intensity outside the zero-level contour of ϕ. The numerator is the summation of intensity values of all pixels outside ϕ and the denominator calculates the total number of pixels outside ϕ. Normally, we have 3 distinct parts for any biomedical medical image. First, the object to be segmented, for example a nodule or tumour, secondly, the organ possessing the abnormality, like lungs for lung nodules, and finally, the region outside the organ captured by the imaging modality which have zero intensity, for example, the region outside the lung field. The following figure 4.6 shows the region of zero information.

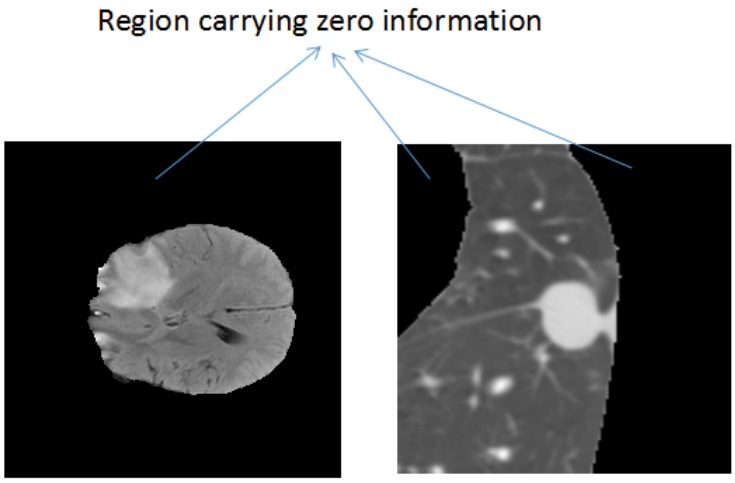

Figure 4.6: Image showing the zero information region of a medical image

For accurate segmentation of an object in a medical image, we need to eliminate this portion of medical image carries zero information. In it very tiresome to manually eliminate such regions, and hence the need of automation. We are providing a formulation, which changes c_2 such that it calculates the average intensity outside ϕ, but within the region of the organ. We modify, c_2 as follows, and denote the new expression as c.

$$c(\phi) = \frac{\int_{\Omega} I(x,y) H(-\phi(x,y)) dxdy}{\int_{\Omega} \{H(-\phi(x,y)) - \delta(I(x,y))\} dxdy} \tag{4.6}$$

where $H(\cdot)$ is one dimensional Heaviside function as defined earlier. In the above defined expression, the numeration calculates summation of intensities outside ϕ and the denominator calculates the number of pixels present outside ϕ, but within the domain of the organ. This achieves the desired average intensity outside phi. For degenerate cases, c is initialized to the average intensity of the organ domain in the medical image. The modified Contrast Adaptive Driving Force term F_{adp} is now given by the following mathematical expression

$$F_{adp}(I,\phi) = g(|\bigtriangledown I_{\sigma}|) \, \textit{sign}\left(I(x,y) - \frac{c_1 + c}{2}\right) \tag{4.7}$$

4.3.2 Shape Variation Force

The shape variation force term is a derivative of an energy functional which computes the area within the zero level contour of the level set function. The effect of this term is to enhance or shrink the speed of evolution based on prior shape information provided for segmentation of an image. The energy functional comprises of three factors

1. Edge indicator function g
2. Heaviside step function $H(\cdot)$
3. Weight factor w

Mathematically, the energy functional is written as

$$A_{\Omega}(\phi) = \int_{\Omega} gwH(\phi) \, d\overrightarrow{\mathbf{x}} \tag{4.8}$$

The role of g is to slow down or stop the growth of zero level contour when it arrives at the object boundaries where it takes smaller values. $H(\cdot)$ is Heaviside step function as described earlier. w is the weight or multiplying factor whose value decides the speed of evolution based on the nature of the object to be segmented. The weight factor w in the equation 4.8 is related to the shape of the evolving contour. The steps involved in the evaluation of the weight factor is discussed in details.

As the zero level set evolves over each iteration, the area and perimeter of this contour increases and its shape changes. The shape of this evolving contour is governed by a *shape factor* which is explained below. Let us consider a specific instance during the evolution of the level set function. Let r_i be the radius of the zero level set in the i^{th} iteration. This radius r_i is a function of three parameters as stated in the following equation 4.9

$$r_i = f(\rho, s, \theta) \tag{4.9}$$

These parameters are defined below

- ρ : Average radius of the evolving contour at each iteration[1]
- s: Shape factor
- θ : Polar angle

[1]Corresponding proof is shown in the Appendix B

The following figure 4.7 illustrates the said theory. r is the distance of the line joining a point on the contour and the centroid, θ is angle subtended on the x-axis by this line.

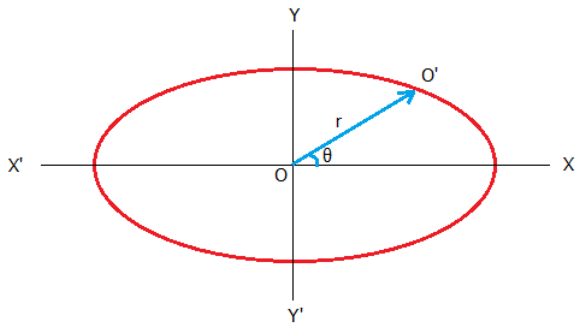

Figure 4.7: Image showing how r_i varies with θ

As evident from the above diagram, the r_i can fluctuate between a minimum and a maximum value for every iteration i. Table 4.1 describes this change as function of angle θ. Shape factor s controls the shape of the level set evolution, such that when $s = 0$ it prioritizes a circular model and when $s = 1$ it prioritizes a non-circular model.
The expression of radius at i^{th} iteration is ideally given as

$$r_i = \rho + s\cos 2\theta \tag{4.10}$$

The following table evaluates radius r_i in terms of ρ and s for some values of θ as per equation 4.10.

$\boldsymbol{\theta}$	$\boldsymbol{r_i}$
0°	$\rho + s$
45°	ρ
90°	$\rho - s$
180°	$\rho + s$

Table 4.1: Radius varying as a function of θ

When θ is an even multiple of $90°$, value of the radius is maximum which is equivalent to the major axis of an ellipse. Similarly, when θ is an odd multiple of $90°$, value of the radius is minimum which is equivalent to the minor axis of an ellipse. For any value of $\theta \neq$ integer multiple of $90°$ the value of radius r_i lies between $\rho - s$ and $\rho + s$. This is how the nature of the evolving contour is governed by the *shape factor*. The *shape factor* directly impacts the circularity, and we have provided a formulation which governs the growth of zero level set based on *shape factor*. To calculate the circularity, we need the area and perimeter of the zero level set. Area of the zero level set in i^{th} iteration,

$$A_i(\phi) = \int_\Omega gH(\phi)\, d\overrightarrow{x} \tag{4.11}$$

Perimeter of the zero level set in i^{th} iteration,

$$P_i(\phi) = \int_\Omega g\delta(\phi) \mid \bigtriangledown\phi \mid d\overrightarrow{x} \tag{4.12}$$

We define *Circularity* in i^{th} iteration of the zero level set as

$$e_{obj} = \frac{P_i(\phi)^2}{4\pi A_i(\phi)} \tag{4.13}$$

$e_{obj} \simeq 1$ for Circular Model and $e_{obj} > 1$ for non circular model[2].

A factor based on the circularity of the evolving contour is formulated as

$$\gamma = \begin{cases} \frac{1}{1+[1-\exp^{-(e_{obj}-1)}]^2}, & \text{if } s = 0 \\ \frac{1}{1+\exp^{-2e_{obj}}}, & \text{if } s = 1 \end{cases} \tag{4.14}$$

The weight is now given as

$$w = (1-s).\gamma + s.\gamma \tag{4.15}$$

The above equation gives the *weight factor* used in our algorithm. This weight w is evaluated in every iteration that suppress or enhance the evolution based on the given priority. Now, once we have established the formulation for the *weight factor*,let us go back to the original equation 4.16. This energy term is minimised by solving a gradient flow, and the resulting equation is given as

$$\frac{\partial \phi}{\partial t} = \beta w g \delta(\phi) \tag{4.16}$$

where β is a scale factor. The right hand side of the above equation 4.16 is our *Shape Variation Force* term and is a function of zero level set and shape factor s. The following equation 4.17 is the mathematical representation of the stated fact.

$$\frac{\partial \phi}{\partial t} = \beta F_{svf} \tag{4.17}$$

where,

$$F_{svf}(s, \phi) = w g \delta(\phi) \tag{4.18}$$

Finally, before we conclude this section, we would like to show the impact of this force term on a synthetic image. The equation 4.17 is implemented to segment an elliptical region. Both the figures are having a different contrast. The resulting difference in contour evolution for two different values of s is shown in the following figure 4.8.

[2]The corresponding proof is given in Appendix C

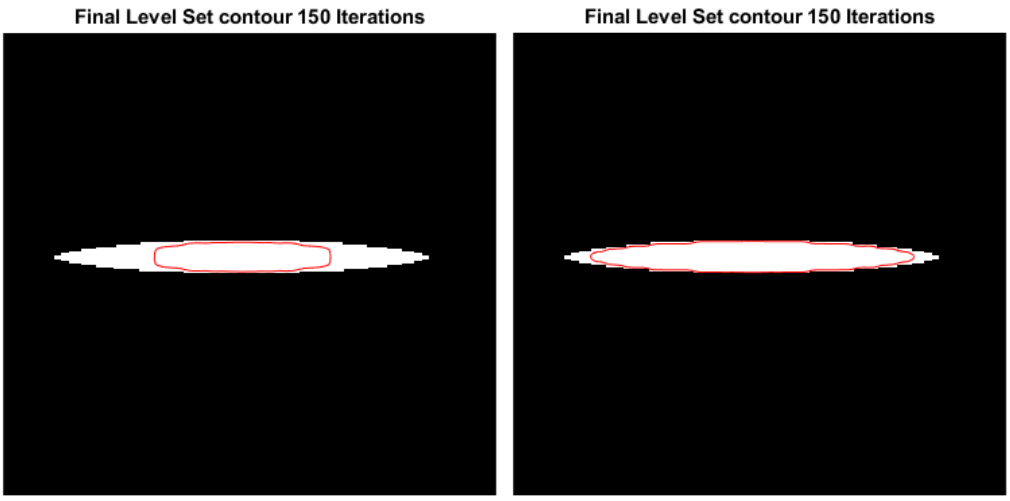

(a) $s = 0$ (b) $s = 1$

Figure 4.8: Evolution based on Shape Priority over an elliptical object

As evident from the above figure, the segmentation is different for two different shape priorities, given the same value of all the remaining parameters. As the object to be segmented is elliptical in nature, the region of interest gets captured when the priority given is elliptical, *i.e.*, $s = 1$. However, the same region of interest, is not getting properly segmented when the priority is circular, *i.e.*, $s = 0$. This is because when the zero level set contour tends to become non-circular in nature, the evolution slows down when $s = 0$ and speeds up when $s = 1$ as per our formulation.

Finally, bringing all the force and regularization terms together, our proposed formulation is given by the following equation 4.19

$$\begin{aligned}\frac{\partial \phi}{\partial t} = \alpha g\left(|\bigtriangledown I_\sigma|\right) sign\left(I\left(x,y\right) - \frac{c_1 + c}{2}\right) + \beta w g \delta\left(\phi\right) + \zeta div\left(d_p\left(|\nabla\phi|\right)\nabla\phi\right) \\ + \nu g\left(|\bigtriangledown I_\sigma|\right) div\left(\frac{\bigtriangledown\phi}{|\bigtriangledown\phi|}\right)\end{aligned} \tag{4.19}$$

Reference

[1] Y. Wang and C. He, 2012. Adaptive level set evolution starting with a constant function. Applied Mathematical Modelling, 36(7), pp.3217-3228.

[2] R. Roy, T. Chakraborti and A. S. Chowdhury, 2019. A Deep Learning-Shape Driven Level Set Synergism for Pulmonary Nodule Segmentation. Pattern Recognition Letters.

[3] C. Li, C. Xu, C. Gui and M. D. Fox, 2010. Distance regularized level set evolution and its application to image segmentation. IEEE transactions on image processing, 19(12), pp.3243-3254.

[4] A. Khadidos, V. Sanchez and C. T. Li, 2017. Weighted level set evolution based on local edge features for medical image segmentation. IEEE Transactions on Image Processing, 26(4), pp.1979-1991.

Chapter 5

EXPERIMENTS AND RESULTS

In this chapter we will focus on the experimental setup and results. We will discuss about the datasets, the performance metrics and the choice of coefficients or parameters used for our experimentation. An internal or ablation study is performed. Our proposed method is also compared with some external state-of-art methods. The system used and the time required for experimentation is also mentioned.

5.1 Datasets

We used three different datasets corresponding to three different category of medical images for our thesis work as mentioned below.

1. *LIDC* for lung nodule segmentation.
2. *BRATS 2015* for brain tumour segmentation
3. *BBBC004* for synthetic cell segmentation.

Apart from the above mentioned datasets, our proposed method was evaluated on Drosophila Kc167 cells (BBBC007 Dataset) , Human HT29 colon-cancer cells (BBBC008 Dataset), Human epithelial type 2 (HEp-2) cells (MIVIA Dataset) and Optic disk (DIARETDB0 & DIARETDB1 Dataset), where our method achieves noteworthy results.

5.1.1 LIDC Dataset

Computed tomography (CT) is being investigated for a variety of radiological tasks involving lung nodules and lung malignancies. Low-dose CT is used as a screening tool for the early detection of lung cancer in high risk populations [1]. To stimulate research and development activities in this area, the National Cancer Institute (NCI) formed the Lung Image Database Consortium (LIDC) [2]. The intent of this database is to hasten advancement of lung nodule CAD research by

1. Providing clinical images to investigators who might not have access to patient images.
2. Creating a reference database that will support the relative comparison of different CAD systems performance, thus eliminating database composition as a source of variability in system performance [3]

LIDC dataset consists of slices of are both low-dose and highdose CT images as well as pre and post-intravenous (IV) in contrast. In LIDC dataset, each slice is a breath-held CT image of the thorax with size 512×512. The number of slices in a stack vary between 95 and 672 and the in-plane pixel size varies between 0.5 and 0.8 mm/pixel. The range for the kVp for these data was 120-140 with 120 as the average and 20.99 as the standard deviation. The range for the mA was 30-634 with 215.9 as the average and 145.1 as the standard deviation. Four different radiologists annotated nodules that were greater than 3 mm in each scan.

5.1.2 BRATS 2015 Dataset

Although many different segmentation strategies have been proposed in the literature earlier, it was hard to compare the existing methods because the validation datasets that are used differ widely in terms of input data (perfusion or diffusion data, structural MR contrasts), the type of lesion (primary or secondary tumours, solid or infiltratively growing), and the state of the disease (pre or post-treatment). So in order to gauge the current state-of-the-art in automated brain tumour segmentation and compare between different methods, Multimodal Brain tumour Image Segmentation (BRATS) challenge was conducted in conjunction with the MICCAI 2015 conference [4]. The datasets of BRATS 2015 contain multisequence MR preoperative scans of patients diagnosed with malignant brain tumours. For each patient, four MR sequences were acquired: T1-weighted, post-contrast (gadolinium) T1-weighted, T2-weighted and FLAIR (Fluid Attenuated Inversion Recovery). The images come from 19 imaging centers and were acquired with different MR systems and with different clinical protocols. The images are provided after the pre-processing performed by the organizers: skull-stripped, registered to the same anatomical template and interpolated to 1 mm^3 resolution. The entire dataset is divided into categories –Training and Testing. The training and testing dataset comprises data from the BRATS 2013 challenge and data from the NIH Cancer Imaging Archive (TCIA) that was prepared as part of BRATS 2014. The Training dataset contains 274 scans (220 High Grade Glioma (HGG) and 54 Low Grade Glioma(LGG)), along with their ground truth segmentation. The 220 HGG comprises of 200 scans from TCIA and 20 scans from BRATS 2013. The LGG comprises of 44 scans from TCIA and 10 scans from BRATS 2013. The Testing dataset consists of 110 scans without ground truth segmentation. Each scan is a stack of 140 slices approximately.

5.1.3 BBBC Dataset

The Broad Bioimage Benchmark Collection (BBBC) is a collection of freely downloadable microscopy image sets. The BBBC dataset provides several benchmarking sets for cell segmentation and counting for many different problems related to image processing in the biological field. These image sets are reference points for developing, testing, and publishing new image analysis algorithms. Also, these image sets themselves include a description of the biological application and some kind of ground truth, namely, Biological labels, foreground and background, outlines of objects and object counts. We have used BBBC004 image set for our experimentation. The BBBC004 image set is aimed at assessing the performance when dealing with clustered cells. This image set consists of five subsets with an increasing degree of overlap among distinct cells. Each image subset includes 20 images in tiff format with a resolution of 950 $\times$ 950 pixels. The images were generated with the SIMCEP simulating platform for fluorescent cell population images.

5.2 Performance Measures

The process for segmenting medical images play an important role in the diagnosis of diseases today, thus the need of a uniform and common framework of performance metrics which are to be used in comparing different algorithms and evaluating their performance [8]. In biomedical image processing, the following are the key terms related to performance measure,

1. False Positive (FP): The model *incorrectly* predicts a pixel belonging to negative class as positive.

2. True Positive (TP): The model *correctly* predicts a pixel belonging to positive class as positive.

3. False Negative (FN): The model *incorrectly* predicts a pixel belonging to positive class as negative.

4. True Negative (TN): The model *correctly* predicts a pixel belonging to negative class as negative.

Based on these definitions, the following performance metrics are defined

1. **Sensitivity**(SE) : Also known as **True Positive Rate** (TPR) is the percentage of true positive pixels correctly identified. Mathematically,

$$SE = \frac{TP}{TP + FN}$$

2. **Specificity**(SP) : Also known as **True Negative Rate** (TNR) is the percentage of false negative pixels correctly identified. Mathematically,

$$SP = \frac{TN}{TN + FP}$$

3. **Accuracy** (Acc): Percent of pixels in the image which were correctly classified. Mathematically,

$$Acc = \frac{TP + TN}{TP + TN + FP + FP}$$

4. **Dice coefficient** (dice): Also known as **Similarity Dice**, is the degree of overlap between the segmented result and the ground truth. Mathematically,

$$dice = \frac{2TP}{2TP + FP + FN}$$

5.3 Parameter Tuning

Tuning parameters to achieve the best result for a given method is an art by itself. Parameter tuning to control the impart each factor in the proposed pipeline is necessary as the success and failure of the method depends a lot on these choice of parameters. There is no method or formula to directly bring out this choice especially when large number of parameters are involved, and we have to depend a lot on visual observation and/or trial and error. However, we do obtain an ideal range of these parameters with the help of graphical method. We plot the dice coefficient for a given parameter, keeping remaining parameters constant.

In our proposed methodology, the key parameters are

1. α : Coefficient of contrast adaptive force

2. β : Coefficient of shape variation force

3. ζ : Coefficient of distance regularization

4. ν : Coefficient of variance regularization

5. $iter$: No. of iterations

The following figures are the plots the variation of the parameters and their effect on dice coefficient, evaluated on LIDC dataset. In every case, $s = 0$, *i.e.*, a circular priority.

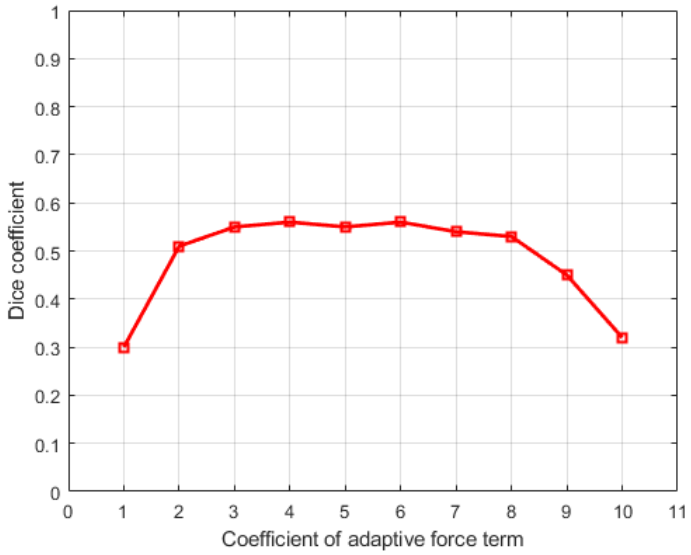

Figure 5.1: α vs dice with $\beta = 5, \zeta = 0.01, \nu = 5, iter = 50$

In the above figure 5.1 we observe that dice coefficient almost remains constant between α = 2 and α = 8. This is because of the fact that the contrast adaptive force term pushes the zero level contour fast towards the edges where it stays indefinitely because of the edge indicator stopping criteria. Between α = 0 and α = 2 propagation takes place of the zero level set and dice coefficient is low due to under segmentation. The fall off beyond α = 8 is because now segmentation of exterior regions, having similar intensity, takes place.

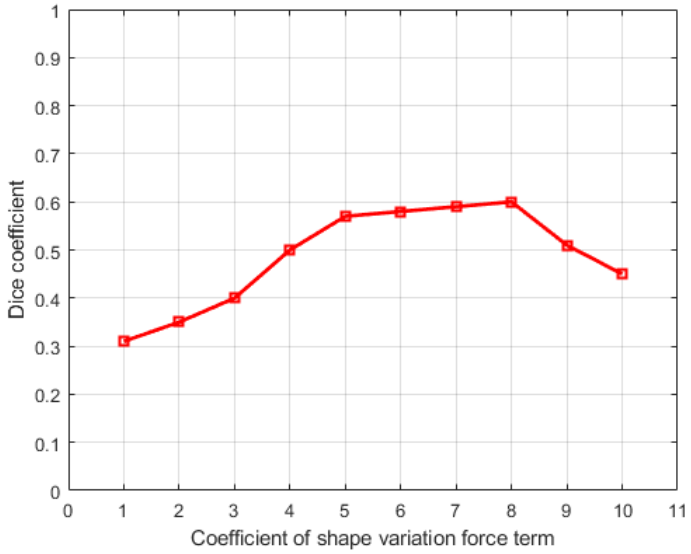

Figure 5.2: β vs dice with $\alpha = 5, \zeta = 0.01, \nu = 5, iter = 50$

In this figure 5.2 shape variation force term is given circular priority. This term moves the zero level set slowly compared to the adaptive force term and hence a slow rise initially. The fall off is due to over segmentation across the edges.

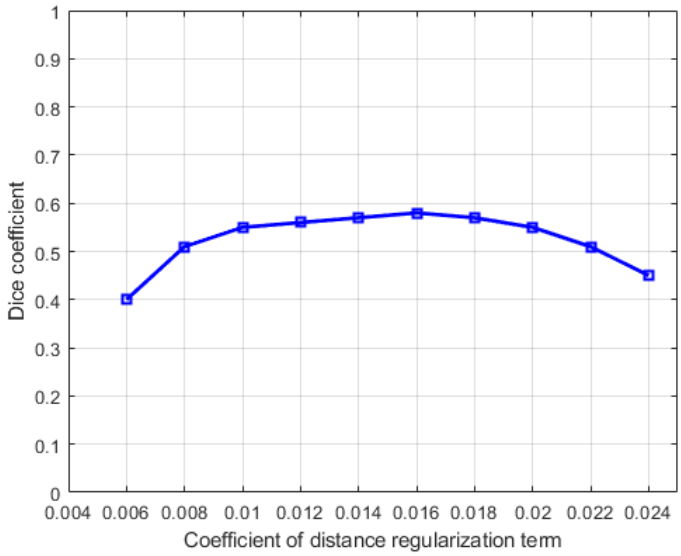

Figure 5.3: ζ vs dice with $\alpha = 5, \beta = 5, \nu = 5, iter = 50$

In the above figure 5.3, distance regularization term is plotted v/s dice coefficient. This term is important as it helps in making smooth evolution avoiding steep and flat surface to crop up and hence reducing numerical errors, thereby an increase in dice coefficient. However, to high a value of this term causes the dice coefficient value to fall off as it now becomes "too strict" and hinders full evolution to reach the edges and hence an under segmentation.

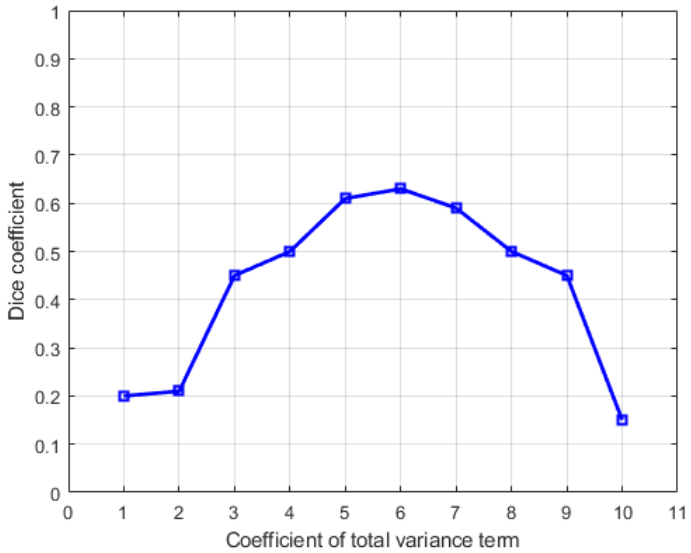

Figure 5.4: ν vs dice with $\alpha = 5, \beta = 5, \zeta = 0.01, iter = 50$

In the above figure 5.4, total variation term is plotted against dice coefficient. The explanation is similar to the that for figure 5.3. Initially, the curve moves up as noise elimination takes place reducing false positives. Higher values suppress evolution.

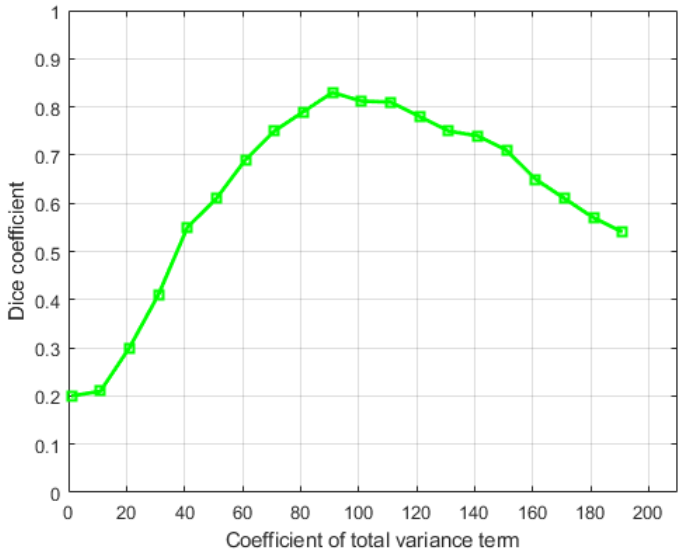

Figure 5.5: $iter$ vs dice with $\alpha = 5, \beta = 5, \zeta = 0.01, \nu = 5$

In the above figure 5.5 dice coefficient is plotted against iteration. The level set contour grows with each iteration, enclosing more and more true positive region, which accounts for the rise in dice coefficient value. Higher iterations causes the dice coefficient to fall off as false positives now starts showing up.

The following figure 5.6 is a 3-D plot where the *x* and *y* axis are the coefficient of two force terms, α and β plotted versus dice coefficient in the the *z* axis.

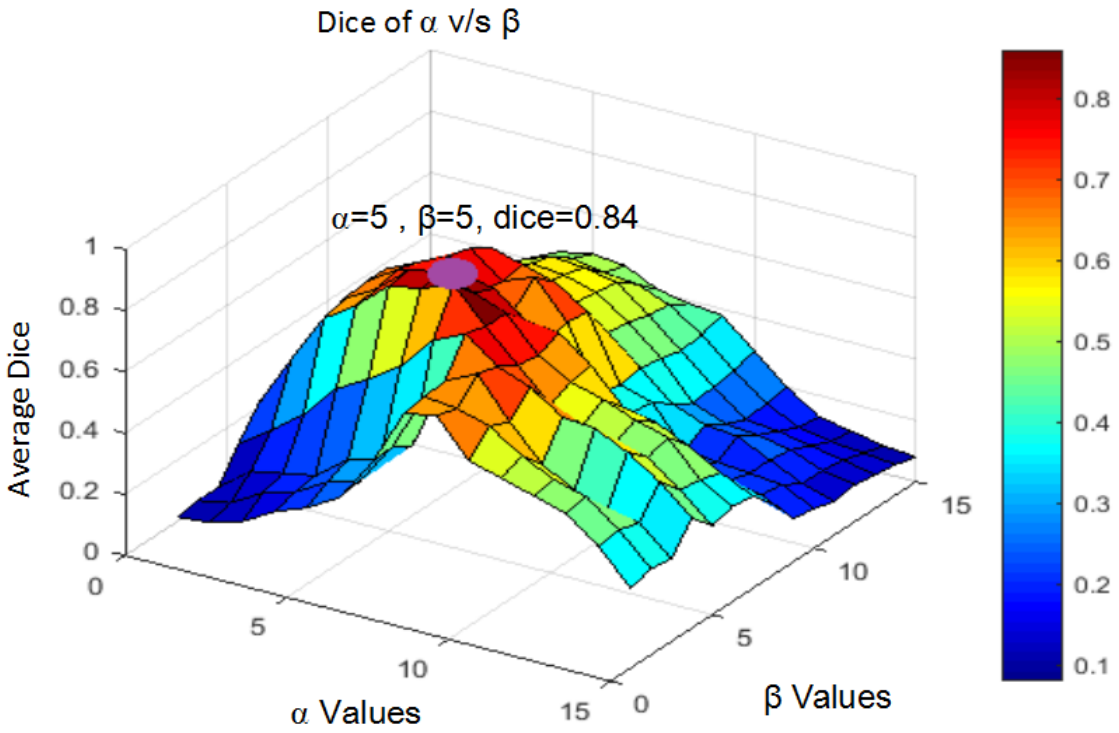

Figure 5.6: 3-D plot showing dice coefficient as a function of α and β

Considering all parameters together and performing extensive calculations, the following values

bring out the best result for lung nodule segmentation over LIDC dataset.

1. α : 5
2. β : 5 with $s = 0$, *i.e.* circular priority.
3. ζ : 0.015
4. ν : 6
5. $iter$: 100

Similar evaluation is done over BRATS dataset where the nature of the curves and their causes are similar. Hence, its not shown simply to avoid redundancy. The same value of the parameters,excluding $iter$ which is now reduced to 80 and s=1 for giving a non-circular priority, obtained best result here. Next, the parameters for segmenting cell image of BBBC004 dataset, take the following values

1. α : 4
2. β : 2 with $s = 1$, *i.e.* non-circular priority.
3. ζ : 0.015
4. ν : 6
5. $iter$: 10

α takes higher values than β as main driving force in case of cells are their intensity and not their shape. The shape of the cells vary not only among different cell images but also within a given image, accounting for the non-circular priority. The value of ν is higher comparatively as the requirement of a sharp distinction because a cell and noise is necessary. $iter$ is reduced comparatively as the area or perimeter of a cell is small and less iterations are needed to reach the boundary.

5.4 Ablation Studies

In the last section we calculated dice coefficient over a certain range of values of a parameter. The main objective of this section is to evaluate the impact of the absence of each of these parameters, keeping the remaining parameters at their precise values. The evaluation is done on a CT slice for lung nodule and an MRI scan for brain tumour. For both lung nodule and brain the initial level set function is Gaussian in nature and the shape driven term is given a circular and elliptical priority respectively. For cell image, the initial level set function is a constant or a step function. Each of the following figures show the segmentation in the absence of a specific term and below them the dice coefficient of the corresponding segmentation result is mentioned. All parameters, except that mentioned below the figure, has the same value as that mentioned in the previous section. At first we consider a CT slice containing of a lung nodule in the figure 5.7 below. In figure 5.7a the segmentation is partial due to the absence of contrast adaptive force term. The evolution is circular in nature clearly showing the impact of a force whose purpose is to evolve the level set function with a circular priority. In the next figure 5.7b, the evolution is intensity based and shape driven term is completely absent. The curve evolves taking the shape of the intensity region. In figure 5.7c, distance regularization term is absent. A close observation reveals the sharp edges of the contour and sight over segmentation towards the right. The

absence of smooth evolution caused numerical error and lowering of dice coefficient. Similarly, in figure 5.7d, another close observation refers the appearance of false positives which is a result of the fact that we are not not able to filter out the noise. The next two figures 5.7e and 5.7f shows the segmentation in presence of all terms, resulting in best dice coefficient value and ground truth respectively.

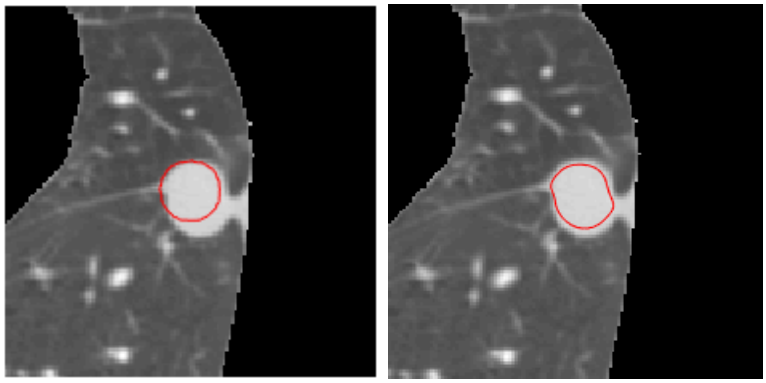

(a) dice=0.67 when $\alpha = 0$ (b) dice=0.69 when $\beta = 0$

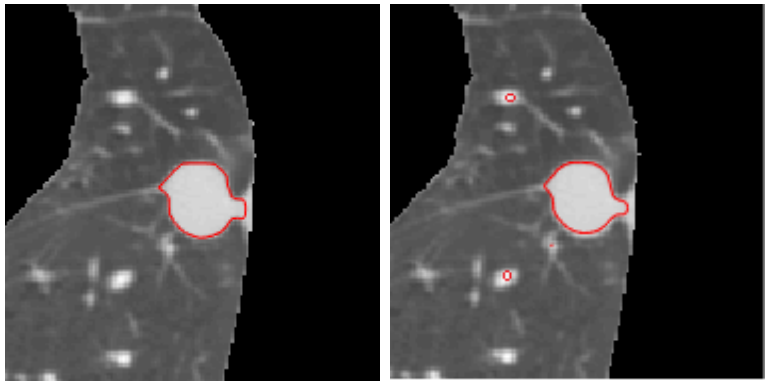

(c) dice=0.71 when $\zeta = 0$ (d) dice=0.74 when $\nu = 0$

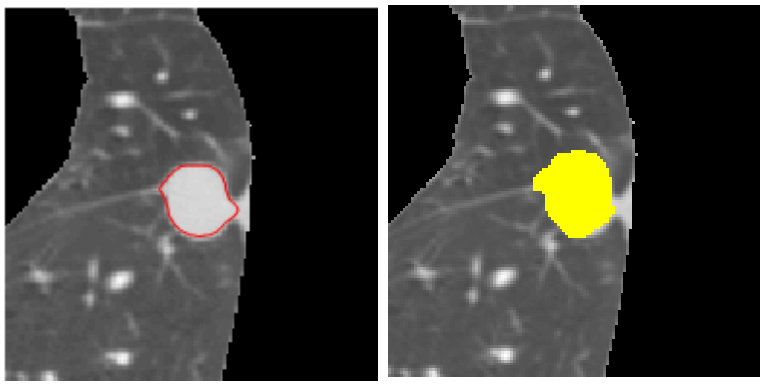

(e) Optimum dice=0.83 (f) Ground Truth

Figure 5.7: Figure show the impact of absence of various terms for segmentation of lung nodules

The following figure 5.8 shows the segmentation on a brain. The previous explanation for lung nodules is also applicable here.

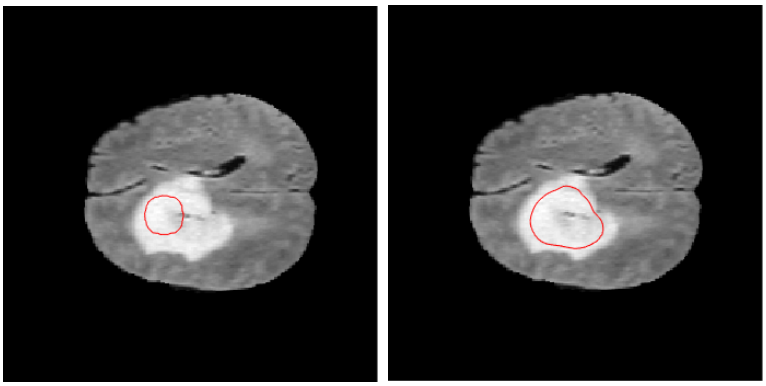

(a) dice=0.3 when $\alpha = 0$ (b) dice=0.71 when $\beta = 0$

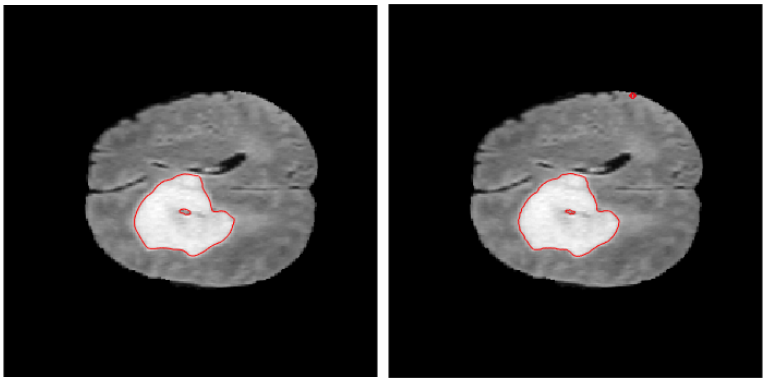

(c) dice=0.80 when $\zeta = 0$ (d) dice=0.79 when $\nu = 0$

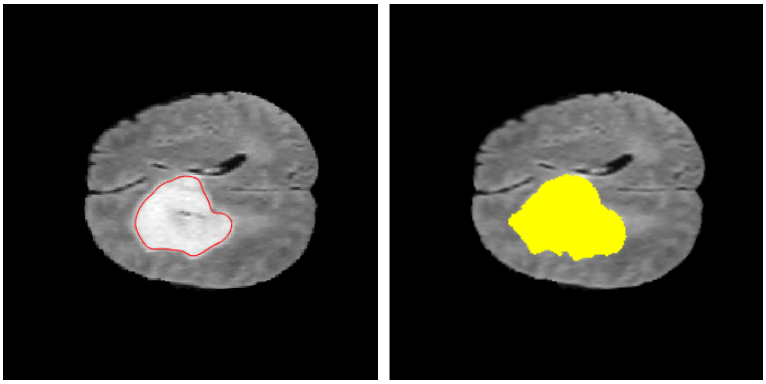

(e) Optimum dice=0.85 (f) Ground Truth

Figure 5.8: Figure show the impact of absence of various terms for segmentation of brain tumour

5.5 External Comparisons

The proposed method is compared with different works as mentioned in the following tables.

5.5.1 Lung Nodule Segmentation

The recent state-of-art methods for lung nodule segmentation are mostly focused in using the potential of deep learning, and non-learning methods with competitive results are hard to find. Our proposed method out-performs several of these methods as shown in the following table 5.1.

Method : Learning based	Dice	Sensitivity	Accuracy
Xie et al. [5]	-	0.86	-
Wang et al. [6]	0.82	-	-
Feng et al. [7]	0.56	-	-
Setio et al. [8]	-	**0.91**	-
Messay et al. [9]	0.77	-	-
Jiang et al. [10]	0.80	-	-
Method : Non-Learning based	**Dice**	**Sensitivity**	**Accuracy**
Zhang et al. [11]	-	0.89	0.94
Ours	**0.84**	0.90	**0.95**

Table 5.1: Dice, Sensitivity, Accuracy comparison with other methods

5.5.2 Brain Tumour Segmentation

The following table 5.2 shows the comparison of our proposed method for brain tumour segmentation with other state-of-art methods. Non-learning methods have achieved competitive results with respect to deep learning. From this table, we observe that minimum and maximum dice coefficient values in case of deep learning based methods are 0.91 and 0.78 respectively, and for non-learning methods its 0.91 and 0.60. Though the maximum is same, the minimum value is lower in case non-learning based methods –reason for dominance of deep learning. Our proposed method also achieves competitive results.

Method : Learning based	Dice	Sensitivity	Specificity
Havaei et al. [12]	0.88	0.87	0.89
Pereira et al. [13]	0.78	-	-
Kamnitsas et al. [14]	0.85	-	-
Mlynarski et al. [15]	**0.91**	-	-
Chen et al. [16]	0.89	-	-
Method : Non-Learning based	**Dice**	**Sensitivity**	**Specificity**
Menze et al. [17]	0.60	-	-
Huang et al. [18]	0.84	-	-
Kwon et al. [19]	0.86	0.86	-
Rehman et al. [20]	**0.91**	-	-
Tong et al. [21]	0.88	0.90	1.0
Ours	0.87	**0.90**	**0.95**

Table 5.2: Dice, Sensitivity , Specificity comparison with other methods

5.5.3 Cell Segmentation

The following table 5.3 shows the comparison of cell segmentation performed over BBBC004 dataset. Unlike lung nodules or brain tumours, cells are much small in size, occur in multiple numbers across an image and overlap in patches. In this table, we are comparing with other methods of cell segmentation, for varying degrees of overlap. In every case, we are achieving competitive results and outperform other methods in terms of accuracy.

Method	Degree of overlap	Accuracy	Sensitivity	Specificity
Khan et al. [22]	0	0.9836	**0.9899**	0.9824
	0.15	0.9858	**0.9875**	0.9856
	0.30	0.9867	**0.9858**	0.9868
	0.45	0.9874	**0.9833**	0.9884
	0.60	0.9888	**0.9857**	0.9901
Riccio et al.[23] (CSC-7)	0	0.9873	0.9552	0.9910
	0.15	**0.9890**	0.9578	0.9924
	0.30	0.9891	0.9559	0.9926
	0.45	0.9895	0.9525	0.9933
	0.60	0.9897	0.9461	0.9940
Riccio et al.[23] (CSC-3)	0	0.9853	0.8798	**0.9975**
	0.15	0.9867	0.8837	**0.9979**
	0.30	0.9861	0.8752	**0.9980**
	0.45	0.9861	0.8703	**0.9982**
	0.60	0.9856	0.8586	**0.9984**
Ours	0	**0.9877**	0.9446	0.9926
	0.15	0.9887	0.9485	0.9931
	0.30	**0.9891**	0.9494	0.9934
	0.45	**0.9898**	0.9525	0.9937
	0.60	**0.9902**	0.9540	0.9938

Table 5.3: Accuracy, Sensitivity and Specificity comparison with other methods

5.5.4 Comparison with other level set methods

We have compared our method with other Level Set based medical image segmentation methods, namely, Distance Regularized Level Set Evolution (DRLSE) [24], Weighted Level Set Evolution(WLS) [25] and Shape Driven Level Set Evolution (SDLS) [26], as shown in the following table 5.4, where we have calculated the maximum and minimum values obtained over LIDC dataset along with the standard deviation.

Method	Min. Dice	Max. Dice	Mean $\pm$ std.
DRLSE [24]	0.28	0.87	0.54 $\pm$ 0.22
WLSE [25]	0.31	0.82	0.66 $\pm$ 0.18
SDLSE [26]	0.61	0.93	0.76 $\pm$ 0.12
Ours	**0.68**	**0.99**	**0.84 $\pm$ 0.10**

Table 5.4: Average Dice coefficient of different Level Set based methods

In the following figures 5.9 -5.13, we are going to show the segmentation results of DRLSE [24], WLSE[25], SDLSE[26] and our proposed method along with the ground truth for each category of nodule.

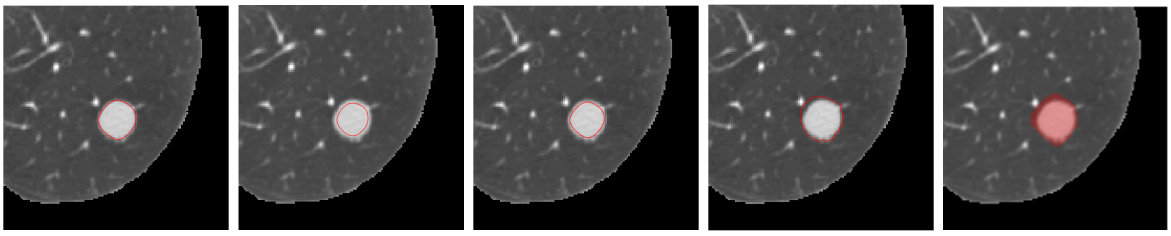

(a) DRLSE (b) WLSE (c) SDLSE (d) Ours (e) GT

Figure 5.9: Segmentation of Solitary Nodule

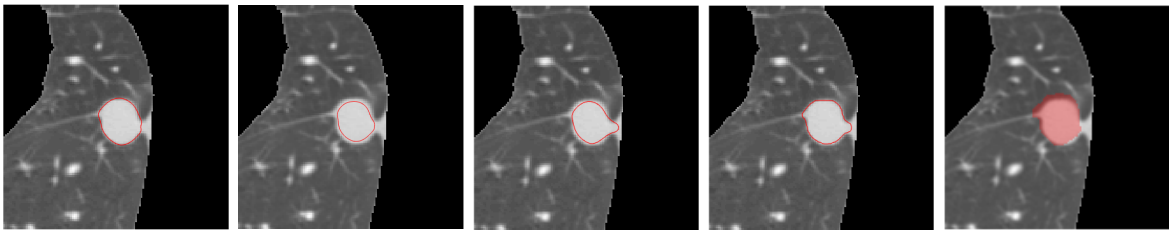

(a) DRLSE (b) WLSE (c) SDLSE (d) Ours (e) GT

Figure 5.10: Segmentation of Juxta Pleural Nodule

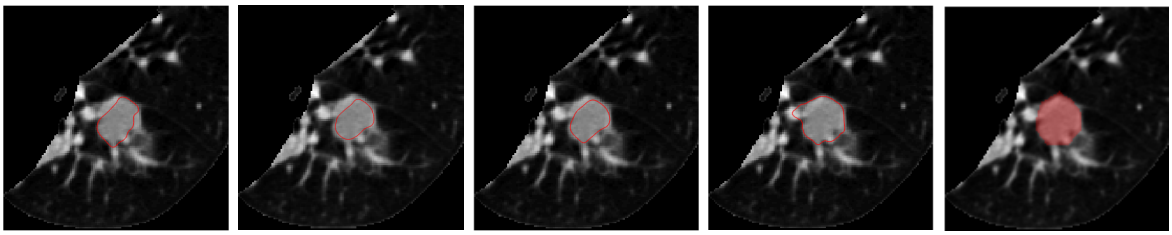

(a) DRLSE (b) WLSE (c) SDLSE (d) Ours (e) GT

Figure 5.11: Segmentation of Juxta Vascular Nodule

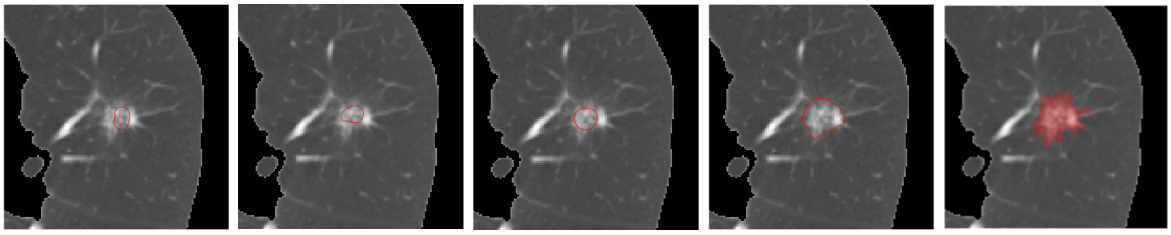

(a) DRLSE (b) WLSE (c) SDLSE (d) Ours (e) GT

Figure 5.12: Segmentation of Part Solid Nodule

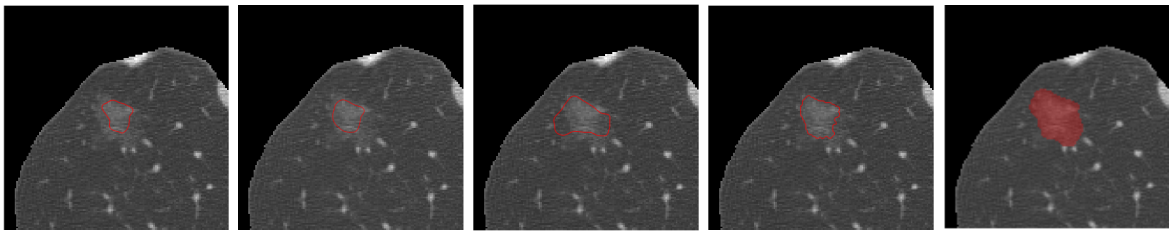

(a) DRLSE (b) WLSE (c) SDLSE (d) Ours (e) GT

Figure 5.13: Segmentation of Ground Glass Nodule

Now, we are going to show the result of the segmentation performed by DRLSE [24], WLSE[25], SDLSE[26] and our proposed method over some MRI slices along with ground truth, in the following figure 5.14

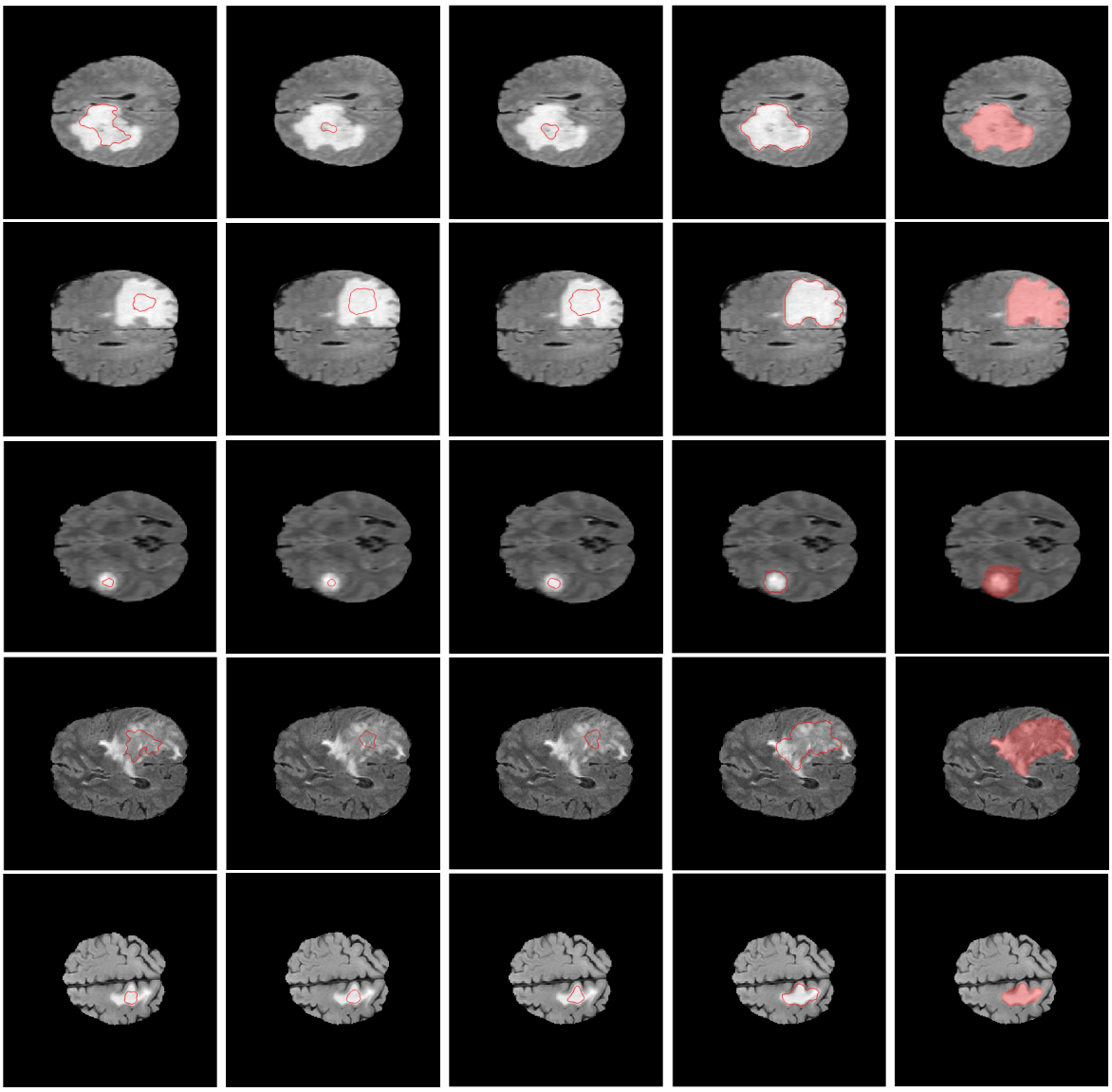

(a) DRLSE (b) WLSE (c) SDLSE (d) Ours (e) GT

Figure 5.14: Segmentation of MRI Slices

Next, we are going show 5 cell segmentation results performed over BBBC004 dataset along with ground truth. Each result corresponds to a particular degree of overlap as shown in the following figures 5.15 - 5.19.

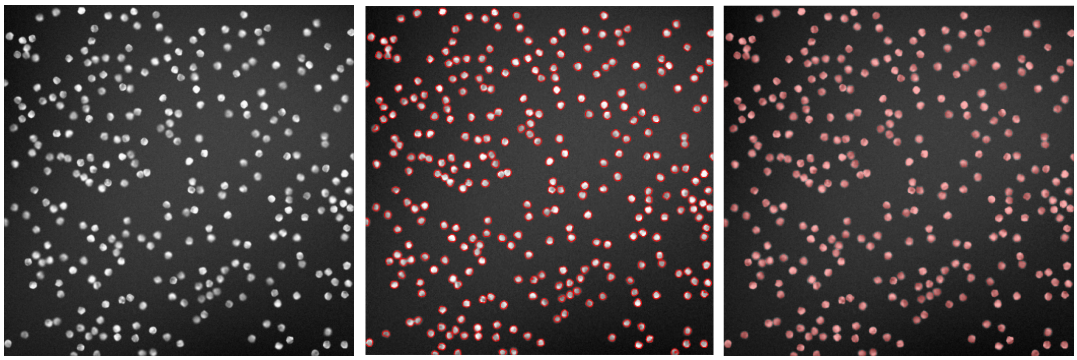

(a) Original Image (b) Segmented Output (c) Ground Truth

Figure 5.15: Cell Segmentation of 0% overlap

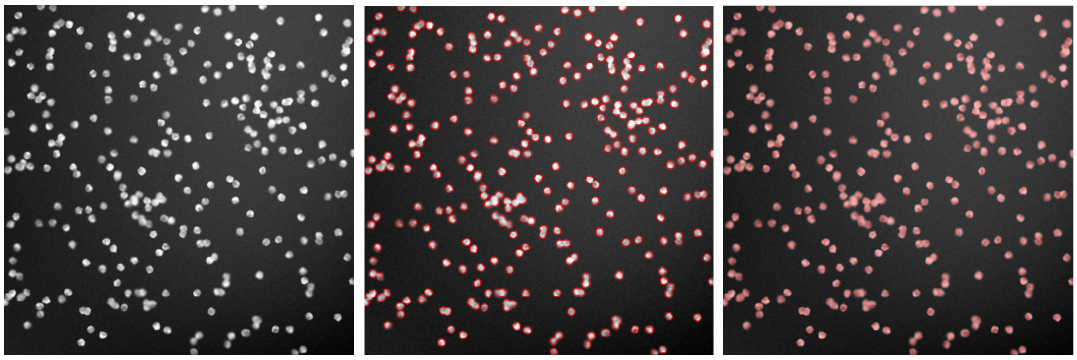

(a) Original Image (b) Segmented Output (c) Ground Truth

Figure 5.16: Cell Segmentation of 15% overlap

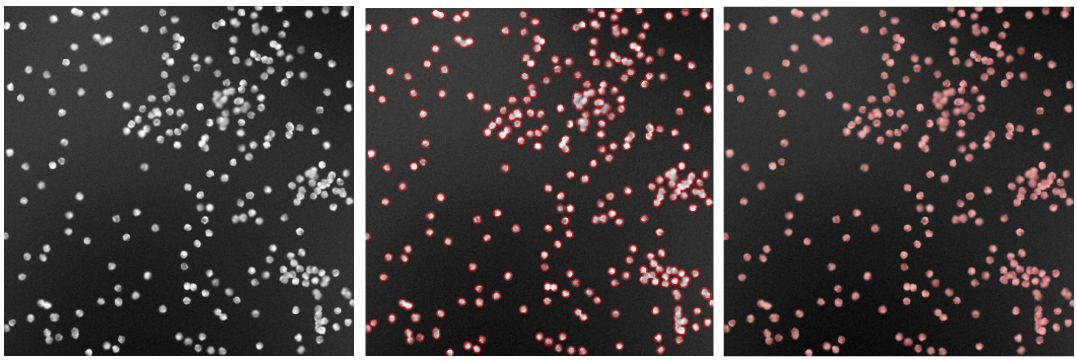

(a) Original Image (b) Segmented Output (c) Ground Truth

Figure 5.17: Cell Segmentation of 30% overlap

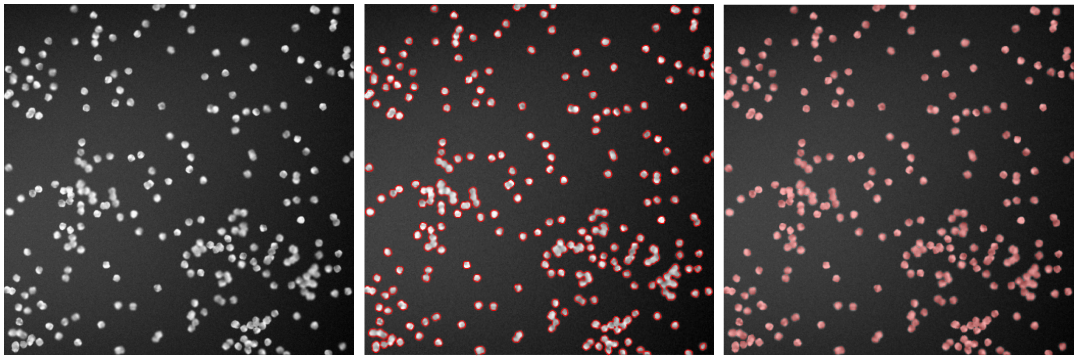

(a) Original Image (b) Segmented Output (c) Ground Truth

Figure 5.18: Cell Segmentation of 45% overlap

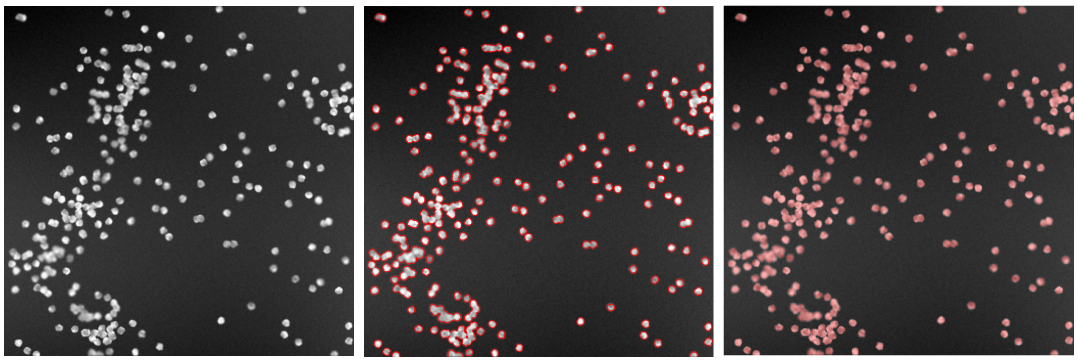

(a) Original Image (b) Segmented Output (c) Ground Truth

Figure 5.19: Cell Segmentation of 60% overlap

5.6 System and Execution time

We have used a desktop PC with 64-bit Operating System, Intel(R) Core(TM) i5-2400 processor with 3.10 GHz speed and 16 GB of RAM for our experiments. We calculated the execution time required by DRLSE [24], WLSE [25], SDLSE [26] with our proposed method, evaluated over LIDC dataset. The result is shown in the following table 5.5.

Method	Execution Time in seconds
DRLSE [24]	331.5
WLSE [25]	1052.1
SDLSE [26]	380.3
Ours	**111.2**

Table 5.5: Execution time of different Level Set Methods

The result shows that our model is much faster compared to other level set models.

Reference

[1] International Early Lung Cancer Action Program Investigators, 2006. Survival of patients with stage I lung cancer detected on CT screening. New England Journal of Medicine, 355(17), pp.1763-1771.
[2] L. P. Clarke, B. Y. Croft, E. Staab, H. Baker and D. C. Sullivan, 2001. National Cancer Institute initiative: Lung image database resource for imaging research. Academic Radiology, 8(5), pp.447-450.

[3] R. M. Nishikawa and L. M. Yarusso, 1998, June. Variations in measured performance of CAD schemes due to database composition and scoring protocol. In Medical Imaging 1998: Image Processing (Vol. 3338, pp. 840-845). International Society for Optics and Photonics.

[4] M. Agn, O. Puonti, I. Law, P.M. af RosenschÃűld and K. van Leemput, 2015. Brain tumour segmentation by a generative model with a prior on tumour shape. Proceeding of the Multimodal Brain tumour Image Segmentation Challenge, pp.1-4.

[5] H. Xie, D. Yang, N. Sun, Z. Chen and Y. Zhang, 2019. Automated pulmonary nodule detection in CT images using deep convolutional neural networks. Pattern Recognition, 85, pp.109-119.

[6] S. Wang, M. Zhou, Z. Liu, D. Gu, Y. Zang, D. Dong, O. Gevaert and J. Tian, 2017. Central focused convolutional neural networks: Developing a data-driven model for lung nodule segmentation. Medical image analysis, 40, pp.172-183

[7] X. Feng, J. Yang, A. F. Laine and E. D. Angelini, 2017, September. Discriminative localization in CNNs for weakly-supervised segmentation of pulmonary nodules. In International Conference on Medical Image Computing and Computer-Assisted Intervention (pp. 568-576). Springer, Cham.

[8] A. A. A. Setio, F. Ciompi, G. Litjens, P. Gerke, C. Jacobs, S. J. Van Riel, M. M. W. Wille, M. Naqibullah, C. I. SÃąnchez and B. van Ginneken, 2016. Pulmonary nodule detection in CT images: false positive reduction using multi-view convolutional networks. IEEE transactions on medical imaging, 35(5), pp.1160-1169.

[9] T. Messay, R. C. Hardie and T. R. Tuinstra, 2015. Segmentation of pulmonary nodules in computed tomography using a regression neural network approach and its application to the lung image database consortium and image database resource initiative dataset. Medical image analysis, 22(1), pp.48-62.

[10] H. Jiang, H. Ma, W. Qian, M. Gao and Y. Li, 2018. An automatic detection system of lung nodule based on multigroup patch-based deep learning network. IEEE journal of biomedical and health informatics, 22(4), pp.1227-1237.

[11] W. Zhang, X. Wang, X. Li and J. Chen, 2018. 3D skeletonization feature based computer-aided detection system for pulmonary nodules in CT datasets. Computers in biology and medicine, 92, pp.64-72.

[12] M. Havaei, A. Davy, D. Warde-Farley, A. Biard, A. Courville, Y. Bengio, C. Pal, P. M. Jodoin and H. Larochelle, 2017. Brain tumour segmentation with deep neural networks. Medical image analysis, 35, pp.18-31

[13] S. Pereira, A. Pinto, V. Alves and C. A. Silva, 2016. Brain tumour segmentation using

convolutional neural networks in MRI images. IEEE transactions on medical imaging, 35(5), pp.1240-1251

[14] K. Kamnitsas, C. Ledig, V. F. Newcombe, J. P. Simpson, A. D. Kane, D. K. Menon, D. Rueckert and B. Glocker, 2017. Efficient multi-scale 3D CNN with fully connected CRF for accurate brain lesion segmentation. Medical image analysis, 36, pp.61-78.

[15] P. Mlynarski, H. Delingette, A. Criminisi and N. Ayache, 2019. 3D convolutional neural networks for tumour segmentation using long-range 2D context. Computerized Medical Imaging and Graphics, 73, pp.60-72.

[16] S. Chen, C. Ding and M. Liu, 2019. Dual-force convolutional neural networks for accurate brain tumour segmentation. Pattern Recognition, 88, pp.90-100.

[17] B. H. Menze, K. Van Leemput, D. Lashkari, T. Riklin-Raviv, E. Geremia, E. Alberts, P. Gruber, S. Wegener, M. A. Weber, G. SzÃľkely and N. Ayache, 2016. A generative probabilistic model and discriminative extensions for brain lesion segmentationâĂŞwith application to tumour and stroke. IEEE transactions on medical imaging, 35(4), p.933.

[18] M. Huang, W. Yang, Y. Wu, J. Jiang, W. Chen and Q. Feng, 2014. Brain tumour segmentation based on local independent projection-based classification. IEEE transactions on biomedical engineering, 61(10), pp.2633-2645.

[19] D. Kwon, R. T. Shinohara, H. Akbari and C. Davatzikos, 2014, September. Combining generative models for multifocal glioma segmentation and registration. In International Conference on Medical Image Computing and Computer-Assisted Intervention (pp. 763-770). Springer, Cham.

[20] Z. U. Rehman, S. S. Naqvi, T. M. Khan, M. A. Khan and T. Bashir, 2019. Fully automated multi-parametric brain tumour segmentation using superpixel based classification. Expert Systems with Applications, 118, pp.598-613.

[21] J. Tong, Y. Zhao, P. Zhang, L. Chen and L. Jiang, 2019. MRI brain tumour segmentation based on texture features and kernel sparse coding. Biomedical Signal Processing and Control, 47, pp.387-392.

[22] H. A. Khan and G. M. Maruf, 2013, May. Counting clustered cells using distance mapping. In 2013 International Conference on Informatics, Electronics and Vision (ICIEV) (pp. 1-6). IEEE.

[23] D. Riccio, N. Brancati, M. Frucci and D. Gragnaniello, 2019. A new unsupervised approach for segmenting and counting cells in high-throughput microscopy image sets. IEEE journal of biomedical and health informatics, 23(1), pp.437-448.

[24] C. Li, C. Xu, C. Gui and M. D. Fox, 2010. Distance regularized level set evolution and its application to image segmentation. IEEE transactions on image processing, 19(12), pp.3243-3254.

[25] A. Khadidos, V. Sanchez and C. T. Li, 2017. Weighted level set evolution based on local edge features for medical image segmentation. IEEE Transactions on Image Processing, 26(4), pp.1979-1991.

[26] R. Roy, T. Chakraborti and A. S. Chowdhury, 2019. A Deep Learning-Shape Driven Level Set Synergism for Pulmonary Nodule Segmentation. Pattern Recognition Letters.

Chapter 6

CONCLUSION

In this work, we present a novel level set method for segmentation of three types of medical images. The zero level set of the proposed level set framework is improved by using three different functions namely a constant function, a step function and a Gaussian function. These three different initialization are used as per the nature of the lesions present in medical images. Constant and step function is used to segment multiple lesions in an image,for instance, cells, and Gaussian function is used to segment single lesion like nodules and tumours. Also, the initialization is robust in nature *i.e.*, the contour evolution of the proposed level set does not depend on the position of initialization. The proposed level set framework mines the intensity and shape information of the image to be segmented in an automated fashion and sets the parameters of the level set. The intensity term is incorporated to handle the segmentation of low-contrast images and it also helps in the segmentation of multiple regions having similar intensity. The shape information is introduced as a weight factor in the proposed level set framework based on the circularity of the evolving contour to prioritize the circular and non-circular lesion to be segmented. This in turn helps in the accurate segmentation of different types of lesions present in the image. Experiments on the publicly available LIDC/IDRI dataset, BRATS 2015 dataset and BBBC dataset clearly reveal that our method achieves promising results compared to several state-of-the-art competitors.

In future, we plan to integrate the proposed model as a layer into a deep learning network. This would automate the initialization of level set method. Another direction of future research will be to embed the shape knowledge in the level set framework for addressing more diverse applications.

Appendix A

Implementation of Proposed Methodology in MATLAB

This section contains the Source Code of our proposed methodology implemented in MATLAB.

A.1 : MAIN CODE - Script File

The script file is executed to obtain the desired output. In other words, this part of the code extracts the input image, makes the required function calls and performs the necessary operation over an image. The script file is given below.

Script file name : IntensityShapeDrivenls.m

```
p_dir=pwd;

% Extraction of Input Image -->

input_image = dir(strcat(p_dir,'\LIDC\'));
input_image(1:2)=[];

% Iteration for growth of Active Contour -->

iter=100;
alp=2.9.*ones(1,1);
wt=zeros(1,1);

for i_no=1:length(input_image)
    in_img = input_image(i_no).name;
    [~,name,ext] = fileparts(in_img);
    Img=imread(in_img);
    figure('Name','Original Image'),imshow(Img)
    [x,y] = getpts;
    Img=double(Img(:,:,1));

%------Initial Level Set as CONSTANT function-------------------%

%       phi0=Constant(Img);
%       phi=phi0;

%------Initial Level Set as STEP function-----------------------%

%      phi0=Step(x,y,Img);
%      phi=phi0;
```

```
%------Initial Level Set as GAUSSIAN function-------------------%

      phi0=Gaussian(Img,x,y);
      phi=phi0;

%------2-D Curve------------------------------------------------%

figure, imagesc(Img); axis off; axis equal; colormap(gray); hold on;
contour(phi, [0,0], 'r');
str='Initial Level Set contour ';
title(str);

%------3-D Surface----------------------------------------------%

figure,mesh(phi);
hold on;
contour(phi, [0,0], 'r','LineWidth',2);
title('Initial level set function');
view([45 30]);

% Edge stopping function -->

 sigma=1.5;
 G=fspecial('gaussian',15,sigma);
 Img_smooth=conv2(Img,G,'same');
 [Ix,Iy]=gradient(Img_smooth);
 f=sqrt(Ix.^2+Iy.^2);
 g=exp(-f./20);

for it=1:iter
     alfa(1,1)=alp(1,1).*(1./(1+(100.*(wt(1,1).^2))));
     wt(1,1)=alfa(1,1);
     sigma=2;
     f0=(1/2/sigma).*(1+cos(pi.*phi/sigma));
     b=(phi<=20) & (phi>=-20);
     diracPhi= f0.*b;
     svf=wt(1,1).*diracPhi.*g;

% Active Contour function Call -->

     [phi,wei,arr,perim,eobj] = ActiveContour(phi,Img,g,svf);
     wt(1,1)= wei;
end

%------Final 2-D Curve------------------------------------------%

figure, imagesc(Img); axis off; axis equal; colormap(gray); hold on;
contour(phi, [0,0], 'r');
str=['Final Level Set contour ', num2str(iter), ' Iterations'];
title(str);
```

```
%------Final 3-D Surface-----------------------------------------------%

figure,mesh(phi);
hold on;
contour(phi, [0,0], 'r','LineWidth',2);
title('Final level set function');
view([60 30]);

% Refining of final contour -->

iter_refine=0;
phi = refine(phi,Img,iter_refine);

%------Saving of Resulting Images--------------------------------------%

cd (strcat(p_dir,'\Output\'))
outputFileName = strcat('output','_',name,'.png');
imwrite((phi),outputFileName,'WriteMode', 'append')
cd (strcat(p_dir,'\'))

end
```

A.2 : FUNCTION FILE CODES

The function files are given below

Function file name : ActiveContour.m

All function codes corresponding to the force and regularization terms, including Neumann's boundary condition are here.

```
function [phi,wei,arr,perim,eobj] = ActiveContour(phi,Img,g,svf)
phi=NeumannBoundCond(phi);
caft=Adaptive_force(phi,Img,g); % Contrast Adaptive Force
vr=Total_Variance(phi,g);       % Variance Regularization
drt=Regularization(phi);        % Distance Regularization
        alpha=5;
        zeta=0.015;
        beta=5;
        neu=6;
        time_step=1;
    phi=phi+time_step.*(alpha.*caft + beta.*svf + zeta.*drt + neu.*vr);
    [wei, arr,perim,eobj] = circ(phi);
end

% Make a function satisfy Neumann boundary condition -->

function g = NeumannBoundCond(f)
[nrow,ncol] = size(f);
```

```
g = f;
g([1 nrow],[1 ncol]) = g([3 nrow-2],[3 ncol-2]);
g([1 nrow],2:end-1) = g([3 nrow-2],2:end-1);
g(2:end-1,[1 ncol]) = g(2:end-1,[3 ncol-2]);
end

% Contrast Adaptive Force Term -->

function f=Adaptive_force(phi,Img,g)

    % Heaviside step function -->

    H=Heaviside(phi,0,Img);

    % Implementation of c1(phi) -->

    Deno_c1_integral=sum(H(:)); % Number of elements within(phi)
    Num_c1=Img.*H; % Intensities in(phi)
    Num_c1_integral=sum(Num_c1(:));
    if Deno_c1_integral ~=0
        c1=Num_c1_integral./Deno_c1_integral;
    end

    % Implementation of c2(phi) -->

    H1=((-1).*H)+1;
    Deno_c2_integral=sum(H1(:));
    Num_c2=H1.*Img;
    Num_c2_integral=sum(Num_c2(:));
    [i1,j1]=size(Img);
    Within_reg_count=0;
    for h=1:i1
        for k=1:j1
            if Num_c2(h,k)~=0
                Within_reg_count=Within_reg_count+1;
            end
        end
    end
if Deno_c2_integral ~= 0 || Within_reg_count ~= 0
    c2=Num_c2_integral./Within_reg_count;
end

 %Degenerate cases -->

if (Deno_c1_integral==0 || Deno_c2_integral==0 || Within_reg_count==0)
  c_temp=(Num_c1_integral+Num_c2_integral)./(Deno_c1_integral
    +Deno_c2_integral);
        c1=c_temp;
        c2=c_temp;
end
```

```
        c=(c1+c2)./2; % Average Intensity
        sign_term=sign(Img-c);

    % Adaptive force term -->

        f=g.*sign_term;
end

% Heaviside function -->

function hf = Heaviside(p, epsilon,image)
hf=ones(size(image)).*(p>=epsilon);
end

%Implementation of Variance Regularization Term -->

function f=Total_Variance(phi,g)
    [phi_x,phi_y]=gradient(phi);
    s=sqrt(phi_x.^2 + phi_y.^2);
    smallNumber=1e-5;
    phi_mag=(s.^2 + smallNumber.^2).^0.5;
    Nx=phi_x./phi_mag;
    Ny=phi_y./phi_mag;
    [nxx,~]=gradient(Nx);
    [~,nyy]=gradient(Ny);
    f=g.*(nxx+nyy);

%Implementation of Distance Regularization term -->

 function f=Regularization(phi)
    [phi_x,phi_y]=gradient(phi);
    s=sqrt(phi_x.^2 + phi_y.^2);
    a=(s>=0) & (s<=1);
    b=(s>1);
    ps=a.*sin(2*pi*s)/(2*pi)+b.*(s-1);
    dps=((ps~=0).*ps+(ps==0))./((s~=0).*s + (s==0));
    f= div(dps.*phi_x - phi_x, dps.*phi_y - phi_y) + 4*del2(phi);
 end

% Divergance -->

 function f = div(nx,ny)
[nxx,~]=gradient(nx);
[~,nyy]=gradient(ny);
f=nxx+nyy;
 end

 % Calculating Circularity factor -->

 function [wei,Ar,Peri,eobj] = circ(phi)
```

```
phi = bwconncomp(phi>0,8);
stats  = regionprops(phi,'Perimeter','Area');
Peri = [stats.Perimeter];
Ar = [stats.Area];
eobj = Peri.^ 2 / (4 * pi* Ar);

% Enhances circular contour evolution -->

wei = 1-exp(-(eobj-0.9));

% Enhances eliptical contour evolution -->

% if eobj < 0.9
%     wei=1-exp(-(eobj-0.9));
% else
%     wei=0.001*exp(-eobj);
% end

end
```

Function file name : Gaussian.m

This function file returns the initial level set function as a Gaussian function.

```
function f=Gaussian(I,x0,y0)
sigma=8; % Should increase for wider spread
ex=@(x,y)((x-x0).^2+(y-y0).^2)./(2*(sigma.^2));
amp=300;
[t1,t2]=size(I);
phi=ones(size(I));
for m=1:t1
    for n=1:t2
        po=ex(m,n);
        phi(m,n)=amp.*exp(-po);
    end
end

initialLSF=phi-280.*ones(size(phi));
f=initialLSF;
end
```

Function file name: Step.m

This function file returns the initial level set function as a Step function.

```
function f=Step(x,y,Img)
    c0 = -2;
    initialLSF = c0.*ones(size(Img));
    initialLSF(round(x(1)):round(x(2)),round(y(1)):round(y(2)))=2;
    f=initialLSF;
```

```
end
```

Function file name: Constant.m

This function file returns the initial level set function as a Constant function.

```
function f=Constant(Img)
a=-2;
f=a.*ones(size(Img));
end
```

Appendix B

This section contains the derivation of the facts stated in section 4.3.2, corresponding to equation 4.9. The following derivation is on the radius at i^{th} iteration. Let r_{avg} be the average radius of the present contour. By convention, the average radius r_{avg} is that value which would yield the same perimeter as that of the contour (with varying radius) for whom it is calculated.

Mathematically,

$$\begin{aligned} 2\pi r_{avg} &= \int_{\theta=0}^{\theta=2\pi} r_i d\theta, \text{ where } r_i \text{ is given in equation 4.10} \\ &= \int_{\theta=0}^{\theta=2\pi} (\rho + s\cos 2\theta)\, d\theta \\ &= \int_0^{2\pi} \rho d\theta + \int_0^{2\pi} s\cos 2\theta d\theta \\ &= 2\pi\rho + s\frac{\sin 2\theta}{2}\Big|_0^{2\pi} \\ &= 2\pi\rho \end{aligned} \tag{6.1}$$

Equating, the right and left hand side of the above equation, we get,

$$r_{avg} = \rho$$

Appendix C

This section illustrates the fact stated through the equation 4.13 in section 4.3.2. For any elliptical contour, we have two values of diameter corresponding to the longest one, say a and shortest one, say b. The area and perimeter is given by,

$$\begin{aligned} Area &= \pi ab \\ Perimeter &= 2\pi\sqrt{\frac{a^2+b^2}{2}} \end{aligned} \tag{6.2}$$

In equation 4.13, circularity factor for ith contour was defined as,

$$e_{obj} = \frac{P_i^2}{4\pi A_i} \tag{6.3}$$

In case of a circle, $a = b =$r(say), so $Area = \pi r^2$ and $Perimeter = 2\pi r$, so that $e_{obj} = 1$
However, when $a \neq b$, circularity is written as

$$\begin{aligned} e_{obj} &= \frac{\{2\pi\sqrt{\frac{a^2+b^2}{2}}\}^2}{4\pi\left(\pi ab\right)} \\ &= \frac{\cancel{4\pi^2}\{\frac{a^2+b^2}{2}\}}{\cancel{4\pi^2}ab} \\ &= \frac{a^2+b^2}{2ab} \end{aligned} \tag{6.4}$$

Dividing both numerator and denominator by b^2, we get,

$$= \frac{\left(\frac{a}{b}\right)^2+1}{2\left(\frac{a}{b}\right)}$$

Let us assume, $\frac{a}{b} = x$. By definition, x varies from 1 to infinity. Let us evaluate e_{obj} for these extreme cases,

Case 1:
When $x \longrightarrow 1$,

$$e_{obj} = \lim_{x\to 1}\frac{x^2+1}{2x} = 1$$

Case 2:
When $x \longrightarrow \infty$, applying L Hospital's Rule,

$$e_{obj} = \lim_{x\to\infty}\frac{x^2+1}{2x} = \lim_{x\to\infty}\frac{2x}{2} = \infty$$

Hence, for all values a x, we get $e_{obj} \geqslant 1$.